CATO-2 Deliverable WP 3.02-D01&D02

D01: Progress report on Calibration and testing of models to experimental data

D02: Progress report on Development of both flow models and flow simulators

Prepared by:	Cas Berentsen,	TU Delft
	Boris van Breukelen	VU Amsterdam
	Johannes Bruining,	TU Delft
	Mariene Gutierrez-Neri,	VU Amsterdam
	Patrick van Hemert (Editor),	TU Delft
	Henk Kooi,	VU Amsterdam
	Colin J. Peach,	U Utrecht
	Panneerselvam Ranganathan,	TU Delft
	E. Susanne J. Rudolph,	TU Delft
	Jon Samuelson,	U Utrecht
	Christopher J. Spiers,	U Utrecht
	Tim Tambach (Editor)	TNO
	Berend A. Verberne,	U Utrecht
	Karl-Heinz A.A. Wolf	TU Delft
Reviewed by:	Pacelli L.J. Zitha (WP leader)	
Approved by:	J.Brouwer (CATO-2 Director)	

1 Executive Summary (restricted)

Successful implementation of CO_2 storage in depleted gas field and saline aquifers requires a detailed design, planning and execution of the storage operations. The knowledge of the physical and chemical processes involved at various time scales is critical for optimizing the storage process and for ensuring long-term safety of the storage sites. The report presents a critical analysis of flow and transport coupled with thermodynamic behaviour and rock fluid interactions for CO_2 storage in depleted gas fields and aquifers. Both CO_2 injectivity and the long term CO_2 migration have been analyzed in detail. The existing models, numerical simulations and experiments have been critically reviewed. The UNIQAC approach has been selected for further development and implementation in the numerical simulation tools. Core-scale modelling and numerical simulations were performed and a workflow for processing CT scan aided CO_2 injection simulations was developed. A detailed design of the CO_2 injection experiments was also done. Samples have been collected for the Bunter sandstone from the TNO core facility and from the Northern Eiffel of Western Germany. The composition of the Bunter sandstone samples has been determined on 4 of the 12 samples. The gas permeability of the Bunter sandstone samples has been determined for most samples. The rest of the analyses are underway.

Distribution List

(this section shows the initial distribution list)

External	Copies	Internal	Copies

Document Change Record

(this section shows the historical versions, with a short description of the updates)

Version	Nr of pages	Short description of change	Pages

Table of Content

2 Applicable/Reference documents and Abbreviations

2.1 Applicable Documents

(Applicable Documents, including their version, are documents that are the “legal” basis to the work performed)

	Title	Doc nr	Version date
AD-01	Beschikking (Subsidieverlening CATO-2 programma verplichtingnummer 1-6843	ET/ED/9078040	2009.07.09
AD-02	Consortium Agreement	CATO-2-CA	2009.09.07
AD-03	Program Plan	CATO2-WP0.A-D.03	2009.09.29

2.2 Reference Documents

(Reference Documents are referred to in the document)

	Title	Doc nr	Version/issue	Date
	Calibration and testing of models to experimental data			

2.3 Abbreviations

(this refers to abbreviations used in this document)

DUT	Delft University of Technology
UU	Utrecht University
VUA	Vrije Universiteit Amsterdam
TNO	Toegepast Natuurkundig Onderzoek
CMG	COMPUTER MODELING GROUP
GEM	GENERAL EQUATION-OF-STATE MODEL
UNIQAC	UNIversal QUAsiChemical thermodynamic model

3 Progress report

3.1 Introduction

Successful implementation of CO_2 storage in depleted gas field and saline aquifers requires a detailed design, planning and execution of the storage operations. The knowledge of the physical and chemical phenomena processes involved various space and time scales is critical for optimizing the storage process and for ensuring long-term safety.

This work-package is primarily concerned with the issues related to the injection of CO_2 in and to the long-term fate of the CO_2 of the selected Dutch demonstration sites. Following discussions with the site-owners, in the first year, the reservoir behaviour focused primarily on the P18 site, located in the Southern North Sea.

This report presents theoretical studies, modelling and numerical simulations and experiments covering the flow and transport coupled with physical-chemical and geo-chemical reactions. Three main observation scales, core-scale, meso-scale and reservoir scale have been considered. The report combines the two deliverables D01 and D02 for the first year of CATO 2 WP 3.02 the two topics of experimental investigation of and modelling of reservoir behaviour are intimately interconnected.

The theoretical work focused on the implementation of state-of-the-art thermodynamic and geo-chemical models for the description of precipitation of minerals and salts and dissolution of rock matrix. The work was mainly done at the DUT, in collaboration with TNO and VUA.

Small scale modelling and simulations were done mainly to make predictions about the core-flood experiments and to develop a work flow for their history-match. This helped design the experiments that are currently under way as part of the second part of the CATO 2 project.

Meso-scale simulations were conducted using a single-phase in-house numerical code built in MATLAB™ developed at the DUT. The simulations done at the DUT were aimed at gaining insight on enhanced mass-transfer due to natural convection combined mineralization, etc and their influence on the long-term fate of the injected CO_2,

Part of the large scale reservoir simulation studies were done also and DUT using the commercial multi-phase simulator of CMG-GEM to investigate large scale effects of CO_2 in generic but practically relevant saline aquifers. The other part was at TNO using first Eclipse 100 or 300 and later using Shell in-house simulator MoRes focusing on the near-wellbore (injectivity, Joule-Thomson cooling) aspects and CO_2 mixing with natural gas for the TAQA P15 and P18 demonstration sites. This simulator was used to model halite precipitation and ensuing injectivity reduction during CO_2 injection in saline aquifers (Muller *et al*., 2009) and proved to be rather robust to capture the coupling of near-wellbore flow combined with phase behaviour.

The experimental study focusing petrological and transport properties of reservoir rocks from the P18 was conducted at the University of Utrecht. This is an essential part of the study of the on the behaviour of the system CO_2 - reservoir rock - pore fluid, under the in-situ conditions of the P18 field that will be continued in the second part of the project.

3.2 Phase-equilibria of aqueous electrolyte solutions

3.2.1 Thermodynamic modelling

Salt or mineral precipitation and dissolution are important processes in the sequestration of carbon dioxide in the underground. A major concern is the possible decrease in permeability near the injection well caused by precipitation of salt or minerals when injecting CO_2 into aquifers or depleted gas reservoirs (see Section 3.1). Note that this is of importance for sequestration both in aquifers as well as in depleted gas reservoirs because a small amount of water is generally present.

Most numerical simulators use simplified models describing the salt and mineral precipitation and dissolution. These models are most likely sufficient for a first estimate. However, it is uncertain whether these models are satisfactory for more detailed predictions and descriptions. This has prompted us to code more accurate models which are also used within chemical engineering to predict/describe salt and mineral precipitation and dissolution. This code will be available for all CATO2 participants.

The code is written in MATLAB^{TM} and allows the calculation of the so-called Gibbs excess energy. The Gibbs excess energy is a measure for the interactions between the molecules forming a system which might consist of various phases such as liquid, solid and gas phase. In chemical engineering the Gibbs excess energy approach is used for the description of phase equilibrium, such as solid-liquid equilibrium as observed when salt precipitates or dissolves, vapour-liquid equilibria and liquid-liquid equilibria. Additionally, chemical reactions can partly also be described using the Gibbs excess energy. The mentioned phase equilibriums and also chemical reactions are all relevant for the description of processes occurring when injecting CO_2 into an aquifer or depleted gas field.

One of the most successful models describing the Gibbs excess energy of an aqueous electrolyte system, is the Pitzer model (1973). Another commonly applied Gibbs excess model is the so-called UNIQUAC model. UNIQUAC is a model which has been developed for the description of the Gibbs excess energy of systems containing uncharged species at various temperatures. Recently it has been adjusted so that also systems containing charged species can be described (e.g., Thomsen (2005)). Both models, the Pitzer model and the adjusted UNIQUAC model are able to capture not only the behaviour of long-range interactions of dissolved ions but also the short-range interactions as encountered for solutions of uncharged species and for high concentrations of charged species.

Fig. 1 shows the first preliminary results of the MATLAB code. In this graph the so-called mean activity coefficient of KCl and of NaCl is given. The mean activity coefficient describes the interactions of the in the water dissolved ions with other ions and with water. The results for NaCl and KCl correspond well with experimental data of Hamer and Wu (1972).

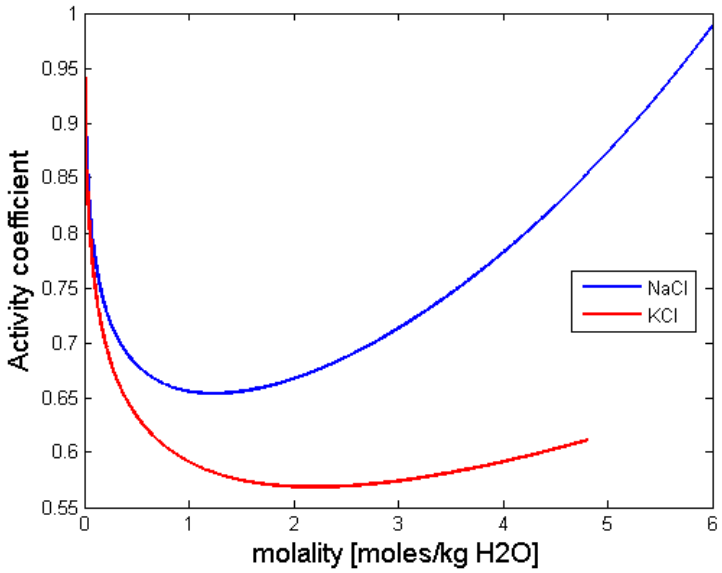

Fig. 1: Mean activity coefficient of dissolved KCl and NaCl in water at 25℃ as calculated by the Pitzer model.

"Abrams and Prausnitz (1975) introduced the so-called *Universal Quasi-Chemical Activity Coefficient* (UNIQUAC) model as a generalization of Guggenheim's quasi-chemical model that accounts for non-randomness to include the effects of molecules of different size" (Tester, 1997). The UNIQUAC model is applicable to multi-component mixtures and has two adjustable interaction parameters per binary (sub-) system. The UNIQUAC model was first used for the description of electrolyte systems by Sander *et al.* (1986). Since then several modifications have been suggested to improve the performance of the model. In this study, the modified version of Nicolaisen *et al*. (1993) will be used.

In the coming weeks, the code of the UNIQUAC Gibbs excess model will be operational and available for the other CATO2 partners. The most important equations are given in Appendix A.

3.2.2 Batch experiments on reaction between reservoir rock and CO_2-rich brine (TNO-Rijswijk)

3.2.2.1 Background, framework & status

When CO_2 is injected in a depleted gas reservoir or aquifer, it will partially dissolve in the water phase (brine) where it will form carbonic acid, thereby lowering the pH. The rock-water-gas system will become out of equilibrium. In order to find a new equilibrium, chemical reactions will occur. If these reactions take place at sufficient high reaction rates, it will change the transport and mechanical properties of the reservoir rock and may affect injection activities and the long-term integrity of reservoir and top seal. Therefore, the rate and impact of reactions between CO_2-rich fluids and reservoir rock is important to investigate. Static experiments on reservoir rocks in contact with CO_2-rich fluids at reservoir conditions can be used to quantify reaction rates and study the impact of reactions on these samples.
This section describes the development of a laboratory facility at the Prins Maurits Laboratory of TNO in Rijswijk. The facility is developed to perform static, long-term reaction experiments

between CO_2-rich brine and reservoir and cap rock as well as wellbore cement, at reservoir conditions. Development of the facility is therefore carried out within the framework of WP3.2 (Reservoir Behavior), WP3.3 (Caprock and Fault Integrity) and WP3.4 (Well Integrity).
An initial test facility was developed and used to carry out reaction experiments between CO_2-rich brine and wellbore cement. These experiments showed that some improvements to the setup were needed to reduce the brine to sample ratio and shield samples from the CO_2-rich brine acting as the pressure medium. Improvements to the setup were needed to reduce the brine to sample ratio and shield samples from the CO_2-rich brine acting as the pressure medium. Improvements to the setup and initial experiments on reservoir rock samples are planned for year 2 of CATO2.

3.2.2.2 Future work

An improved experimental setup is being developed which allows experiments with a more realistic brine to cement ratio. In the improved setup an additional sample is place between an upper and a lower stainless steel piston in an EPDM and FEP jacket and positioned next to a sample in the original sample configuration. Within the vessel a sample in the initial configuration can run simultaneously with a sample in the improved configuration in order to compare the two methods and to investigate the effect of the improved facility. A connection between the supercritical CO_2 in the open vessel and the jacketed sample is possible to allow equal CO_2 pressure and vaporized water content in both experimental settings. The connection can also be closed in case a lower pressure is required in the jacketed sample to prevent leakage through the jacket. Experiments will have to show whether it is necessary to open the connection to prevent drying out of the jacketed sample and whether leakage in the jacketed sample will occur if the connection is opened. Brine samples can be taken during the experiment through the bleeding/sampling tap. The jacketed sample method is similar as used by Liteanu (2009) and therefore comparison of experimental results is allowed. The improved setup will be used to perform experiments on representative samples of reservoir rock and brine compositions (planned for year 2 of CATO-2).

3.3 Experiments and modelling of core floods

3.3.1 Modelling of the CO_2 injection experiments

Near-wellbore modelling and numerical simulations have shown that significant loss of well injectivity may arise due to salt precipitation during CO_2 injection saline formations (e.g., Carpita *et al.*, 2006; Muller *et al.*, 2009). Nevertheless, lack of reliable experimental data on salt precipitation and its effect on rock-fluid physics has hindered accurate modelling and simulation of field for operations (Hurter *et al.*, 2007).

In order to investigate the effect of the interaction of CO_2 and brine in depleted gas fields or in aquifers, we plan to conduct core flood experiments. In these experiments CO_2 will be injected in sandstone cores from the TAQA P15 or P18 locations or in selected analogues thereof. The cores will be either fully saturated with brine or will contain brine and methane to simulate natural gas. In addition to standard pressure drop and effluent volumetric measurements CT scans of the core will be done in the experiments to determine the fluid saturations and concentrations of eventually deposited minerals.

For all experiments, numerical modelling of the experiments will be done: (a) before the experiments to predict the CO_2 flow and mineralization behaviour based on the presumed rock-fluid phenomena, injection rates, etc. and aid the overall design of the testing conditions (b) after the experiments, as part of the history-matching of the experimental data and to verify the assumed CO_2 mineralization mechanisms.

In this report we present preliminary simulation results for a Bentheimer sandstone core (4.0 cm diameter and 17.0 cm length, average ϕ = 20% and k = 1200 mD) obtained using the Compositional Equation-of-state Model of Computer Modelling Group (CMG-GEM) simulator, As a base case we consider the injection of CO_2 in the core previously saturated with brine with a flow rate of 5.0 cm^3/min. The outlet pressure is kept constant at 10 bar and temperature is equal to 50 ^{0}C. Under these conditions the CO_2 will be in the gas phase (Bachu and Adams, 2003).

Fig. 2 shows the schematic of the work flow that we have developed processing of the experimental data. First the dry and brine saturated cores are CT scanned. By subtracting the corresponding CT images we obtain 2D porosity maps of the sandstone sample. The slices are collation concatenated to form a 3D numerical core model. The number of voxels (volume pixels) is to large to be used as obtained from the CT scans as it would lead to rather long computations times. Since we would like to repeat the simulations for varying parameters, the core model is reduced using simple up-scaling technique.

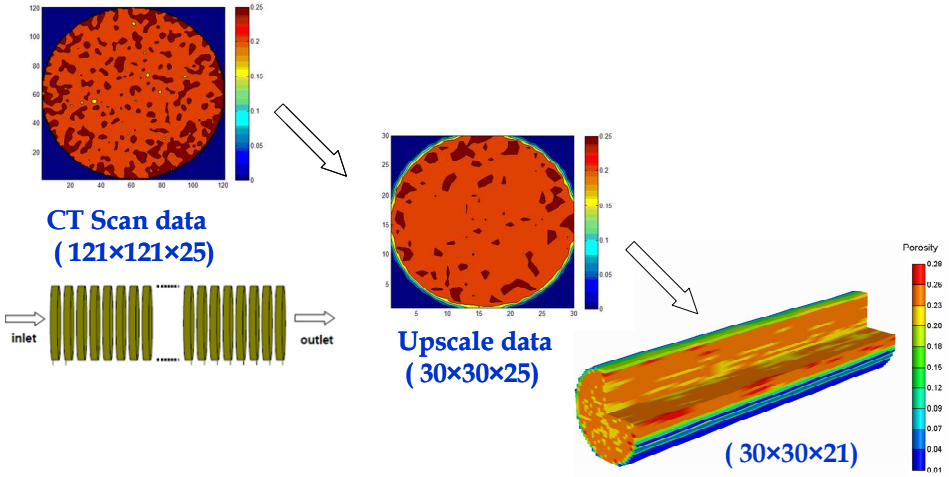

Fig. 2: First the dry core (11 is scanned and by generate a numerical template of the core. The number of voxels (volume pixels) is reduced using an up-scaling). The up-scaled core is used for detailed modelling and numerical simulations.

The absolute permeability field is derived from the porosity map using porosity-permeability (k-ϕ) correlations. In this work the Kozeny-Carman (Bear, 1972) and fractal geometry (Pape et al., 1999) k-ϕ correlation tested in order to match the spatial distribution of the injected CO_2. The relative permeability of gaseous CO_2 and brine were modelled using the Brooks-Corey correlations (Bear, 1972) while the capillary pressure is modelled using the van Genughten (1980) correlation. The Peng-Robinson equation of state (Peng and Robinson, 1976) was used to describe the thermodynamic behaviour of the CO_2 brine mixture. Other equations of state will be used in the future for the more complex CO_2-hydrocarbon gas-water mixtures. The Pederson viscosity correlation (Pederson et al., 1984) was used to describe the dependence of viscosity on pressure and temperature.

Fig. 3 shows saturation maps obtained at different simulation times for an injection in a horizontal core. As could be inferred from the density differences between gas and brine densities significant gravity segregation can be observed. As CO_2 propagates towards the outlet it is also pushed downwards leaving over time only a small part of the core un-swept.

To check whether we can eliminate gravity segregation at the specified flow conditions we also simulated CO_2 injection in a vertical direction either upwards or downwards. Fig. 4 shows the resulting CO_2 saturation maps at 50 min. The horizontal case is also shown for comparison. The simulations show that the horizontal case provides earliest CO_2 breakthrough. For the two vertical cases CO_2 is distributed more uniformly over core cross-sections. The up-water injection is characterized by fingering while downward injection is gives a front like propagation of CO_2. Since the aim of the CO_2 experiments is to isolate the effects of CO_2 interaction with brine and mineralization it was concluded on the base of these results that experiments will be done vertical under gravity stable conditions.

Follow-up modelling and simulation will focus on: a) CO_2 mass transfer into the brine and the ensuing mineralization, b) investigation of the various sensitivities and c) develop an automated history-matching procedure, d) modelling of the CO_2 is rocks containing natural gas.

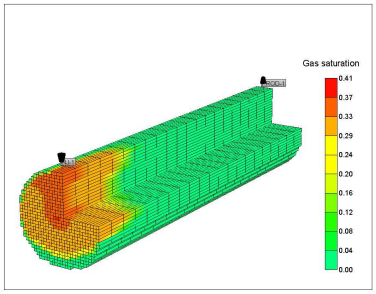

10 min

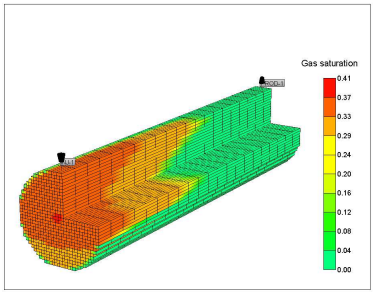

25 min

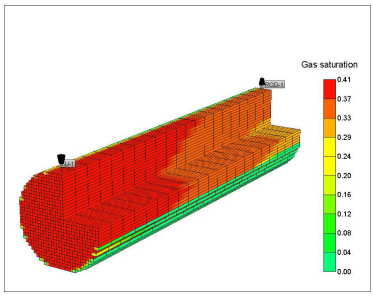

50 min

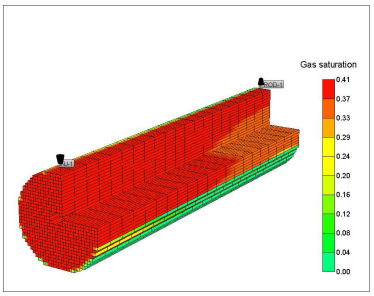

100 min

Fig. 3: Saturation maps obtained after 10, 25, 50 and 100 minutes for CO_2 injection in a horizontal sandstone core.

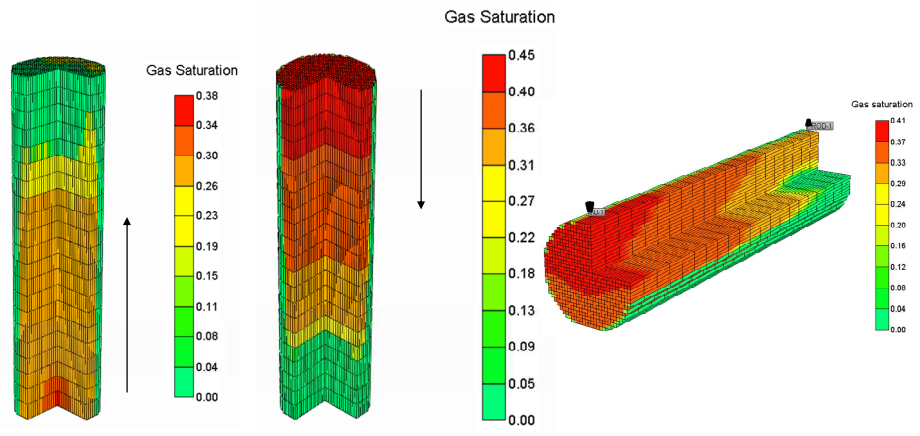

a) b) c)

Fig. 4: CO_2 saturation profiles at time of 50 min for: a) vertical with upward direction b) vertical with downward direction c) horizontal.

3.3.2 CO_2 injection experiments

As mentioned above, the injection of CO_2 into aquifers or depleted gas fields is accompanied by a number of processes which influence the field-scale behaviour. One of these processes is permeability reduction due to the precipitation of salt and minerals. Precipitation of salts and minerals in porous medium depends on the properties of the formation rock, the composition of

the formation fluids and the interactions between rock, fluids and the injected CO_2. Even though the precipitation and dissolution of salts and minerals in aqueous electrolyte (bulk) solutions is well understood, the behaviour in porous medium at reservoir conditions is not well understood and experimental data is lacking. In particular, it needs to be identified how these processes, occurring at micro/pore-scale, influence field scale behaviour and how they can be coupled to the description of permeability.

For the formulation and validation of models describing this permeability behaviour, experimental data will allow the identification of the principle processes. In order to obtain this data, new experimental set-ups are being constructed and existing experimental set-ups are being modified. The planned experiments will:

- visualize the precipitation of salt induced by the injection of carbon dioxide (see section 3.3.3)
- study the decrease in permeability due to the precipitation of salt induced by the presence and flow of carbon dioxide(see section 3.3.5)
- gain fundamental insight into the physical-chemical aspects of water displacement by CO_2 injection (see section 3.3.4)
- obtain capillary pressure curves of carbon dioxide, (saline) water and reservoir rock when injecting CO_2. Details of the set-up are discussed in the CATO2 WP3.03 D09 progress report.

3.3.3 Visualization of precipitation of salt

For the description of permeability reduction due to salt/mineral precipitation it needs to be identified where and how the salts/minerals precipitate in the porous medium. Experiments with non-destructive visualisation will be performed to obtain information on the location and amount of salt precipitation due to flow of carbon dioxide through a sandstone core partially saturated with saline water. This section is the experimental part of the work presented in section 3.3.1.

In Fig. 5 the experimental set-up for the core flood experiments is shown. As non-destructive visualisation method CT- and micro CT-scanning will be used. While CT-scans can also be done during an experimental run, the higher resolution micro-CT scans will only performed after the actual experiment on parts of the core. A small sample of the core will be analysed before and after the experiment using XRD analysis to determine variations in the composition of the core and the precipitated salt. The set-up will allow the injection of supercritical CO_2 into a sandstone core with a maximum length of 40 cm and a diameter of 14 cm. The set-up depicted in Fig. 5 will be completed and up for running by end of October.

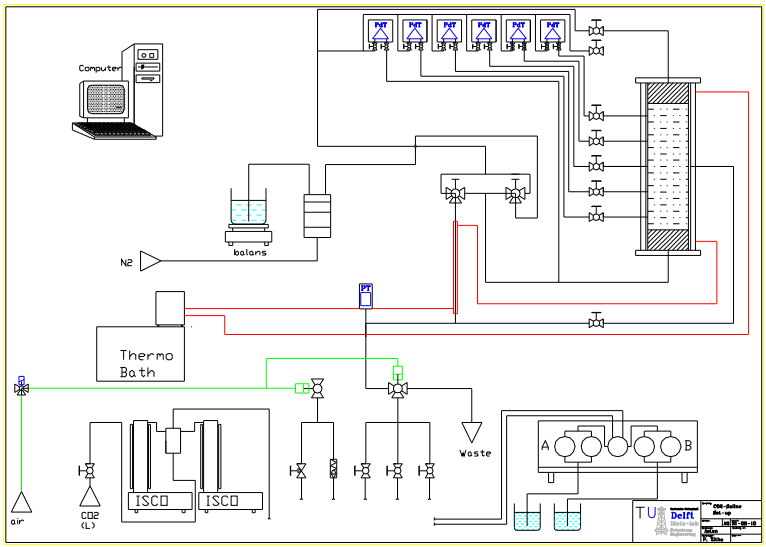

Fig. 5: Schematic drawing of the experimental set-up.

3.3.4 Long-tube experiments

Estimation of the behaviour of CO_2 injected into aquifers and depleted gas fields is based on experiences, principles and experimental data relevant for the oil and gas industry. Earlier experimental studies have indicated that injection of CO_2 in brine-saturated rock samples leads to salt precipitation and thus to permeability reduction (Wang *et al*., 2009). Halite precipitation during gas injection was investigated by several authors (Wang *et al.*, 2009; Zuluaga and Monsalve, 2003; Zuluaga *et al.*, 2001). However, data describing the displacement of (formation) water by CO_2 are scarce but are crucial for the design and for operating a CO_2 subsurface storage installation. Data on the diffusion into and dispersion of CO_2 in bulk water can be found. However, the water displacement by CO_2 and the diffusion of CO_2 into the water, and vice versa, in a porous medium, cannot be described reliably based on these data. Not all factors influencing these processes in porous medium are considered when studying 'only' the bulk phase behaviour.

Long-tube experiments are being designed to investigate the behaviour when injecting CO_2 into an aquifer or a depleted gas field. These experiments provide insight in the physical-chemical processes occurring when CO_2 is injected into a reservoir. The influence of temperature and pressure on the following properties and processes in porous medium need to be understood:

- mass transfer by dissolution/diffusion of CO2 in water phase, and vice versa
- Two-phase displacement behaviour including the spreading of CO_2 in aqueous phase caused by diffusion, dispersion and retardation effects
- The sensitivity of aforementioned measurements to the dimensions of the tube (length + diameter).

Better insight in the processes allows improving the numerical models with respect to

- Influence of temperature and pressure on the length of the transition zone of the CO_2-water displacement process
- efficiency of specific reservoirs with respect to CO_2 storage

- "drying out" effects of porous medium due to injection of CO_2
- fractional flow of water and CO_2

In addition, the better insight will allow the formulation of an improved CO_2-water phase behaviour model.

Quantities that directly experimentally determined are:

- Determination of salt and CO_2 content in the aqueous phase (in-situ and in outflow)
- Determination of the water content in gas phase (in outflow)
- "Length" of the CO_2-saline water inter-phase ('mixing' zone) as function of time, injection rate, temperature and pressure
- Diffusion and dispersion behaviour of CO_2 in aqueous phase
- Alterations of porosity and permeability due to precipitation

Commercial slim tube experimental set-ups (see e.g. Fig. 6), cannot be used, because

- The curvature of the tube biases the (longitudinal) mixing behaviour
- Wall effects have a non-negligible effect on the displacement behaviour because of the small diameter of the tube (variance of the velocity field, asymptotic Taylor dispersion)
- The amount of CO_2 dissolved in the aqueous phase cannot be visualised in-situ at various locations.
- Slim-tube dimensions cannot easily be varied.

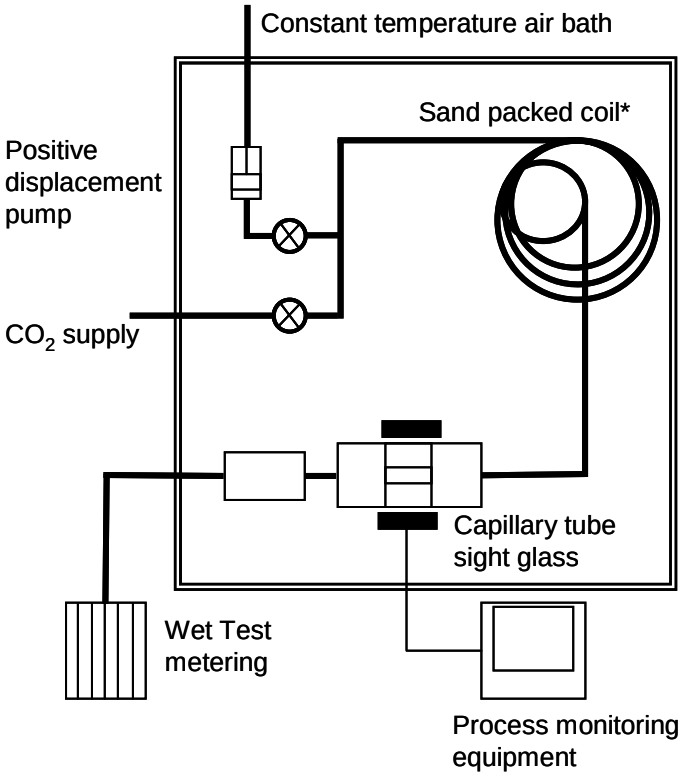

* 6.35 mm O.D. stainless steel tubing 12.2 meter long, packed with 160-200 mesh Ottawa sand

Fig. 6: Schematic drawing of a commercial slim-tube apparatus

To overcome the aforementioned issues a new apparatus is being developed. Fig. 7 is the first draft of the design of the equipment. The main challenge is to find a non-destructive fast and accurate visualization technique that allows also quantification of in situ properties such as concentration, saturation and changes in the mineral content. Techniques that are currently evaluated are:

- Instrumental Neutron Activation Analysis
- Mass Spectrometry (only effluent measurements)
- Mobile CT-scanner (limited resolution)
- SESANS: Spin-echo small-angle neutron scattering
- Nuclear magnetic resonance scanning
- Spontaneous (or self) potential
- Spectroscopy

Another major experimental challenge is the construction of a fluid phase separator at the outflow so that the concentrations of dissolved CO_2 and salt in the aqueous phase can be determined at reservoir temperatures and pressure. Other important aspects are the temperature control over the complete length of the tube, orientation of the tube allowing to vary dip angle, filling procedure of long tube with loose sand (or glass beads).

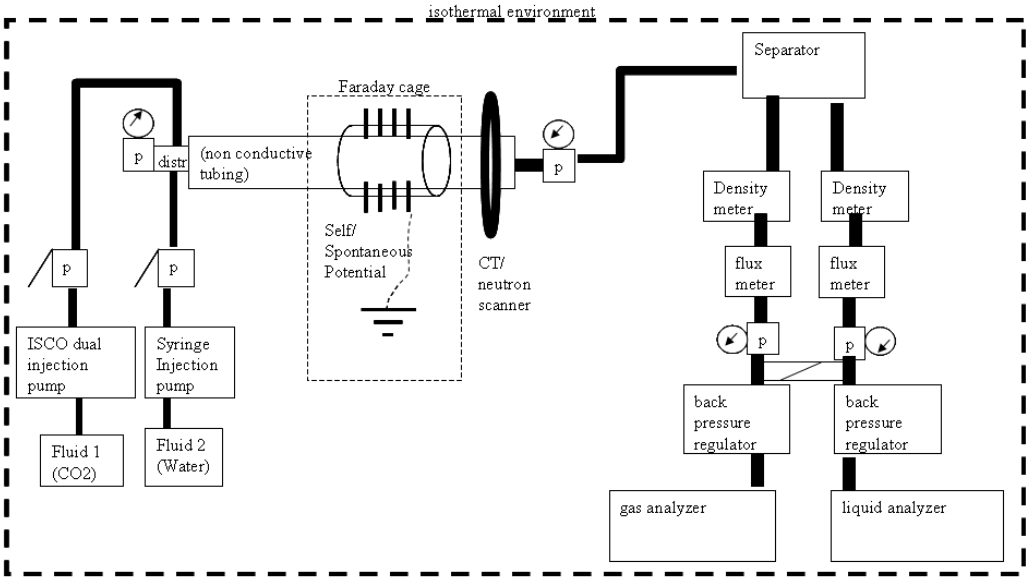

Fig. 7: Preliminary schematic overview of long-tube experimental set-up.

3.3.5 Permeability reduction due to salt precipitation

Courtesy of Giacomo Bacci and Sevket Durucan (Imperial College London, GRASP project)

Precipitation of salts and minerals in porous medium depends considerably on the properties of the formation rock and formation fluids as well as the interactions between rock, fluids and the injected CO_2. Even though the precipitation and dissolution of salts and minerals in aqueous electrolyte (bulk) solutions is well understood, the behaviour in porous medium at reservoir conditions is not well understood and experimental data are lacking. Therefore, laboratory

experiments that investigate the reduction in permeability due to precipitation of salt induced by the flow of carbon dioxide are required.

A set-up (Fig. 8), similar to the one used by Wang *et al.* (2009), has been constructed that allows the injection of supercritical carbon dioxide into a rock core sample. An ISCO pump is used to saturate the core with saline water, to determine the permeability and to inject CO_2. Displaced saline water and water vapour are collected at the outlet of the core will be collected using a water trap at the outlet of the set-up. This set-up has been assembled and is ready for use. A first set of experiments have been performed on sandstones and carbonates for another project (GRASP). Results are presented in Bacci *et al*. (2011).

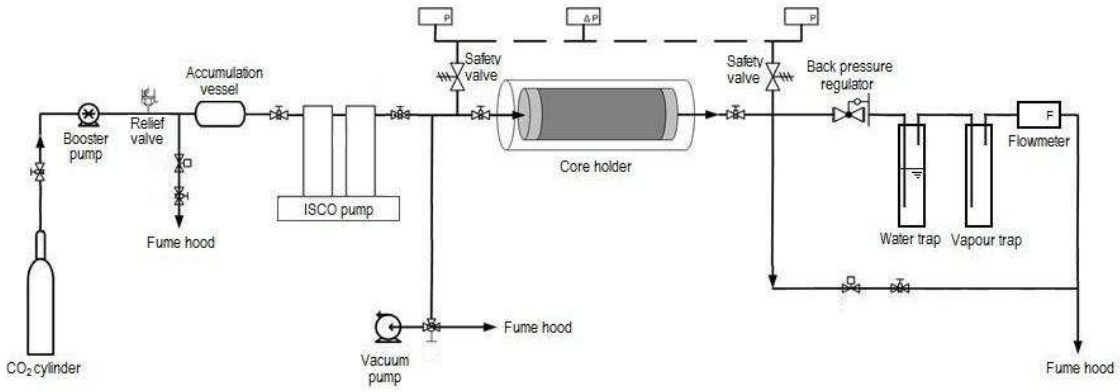

Fig. 8: Experimental set-up for the investigation of permeability reduction due to salt precipitation (Bacci *et al*., 2011).

3.4 Petrological and chemical studies for the P18 Bunter sandstone

3.4.1 Introduction

In this contribution we report our progress regarding the preliminary experimental work performed in Year 1 of CATO-2, within Work Package 3.2. Our aim in this period was to determine the petrological and transport properties of P18 reservoir rocks (P18 field, Southern North Sea), and to initiate work on the behaviour of the system CO_2 – reservoir rock - pore fluid, under the in-situ conditions of the P18 field. To this end we have conducted thin section analysis of core material, and are still in the process of doing X-ray diffraction analyses, permeametry and fluid-rock reaction experiments. The data produced will provide a basis for constructing, calibrating and testing models of the effects of reaction and reactive transport on reservoir rock composition, microstructure, permeability and mechanical properties.

3.4.2 P18 reservoir rock samples: composition and microstructure

The P18 reservoir rock samples used as starting material in this study (samples 1 to 7 in table 1), were collected from the TNO core repository in Zeist. They originate from wells P18-02-A1 and P18-02, located within field P18, from different stratigraphic levels in the Bunter sandstone formation (Table 1). In the Netherlands this formation is known as the Main Buntsandstein, and further subdivided into the Volpriehausen, Detfurth and Hardegsen formations, and, locally, the Basal Solling sandstone. Where possible, we collected 25 mm diameter cylindrical cores of 60 mm maximum length both perpendicular and parallel to the sedimentary layering. These were respectively designated with a suffix ‘a’ and ‘b’ (Table 1). Because of limited sample availability we also performed a field excursion to the Northern Eiffel of Western Germany, where the Main Buntsandstein is interpreted to be equivalent to that of field P18 (Ames and Farfan, 1996). Consequently, two other samples, 16E and 17E, were collected from different outcrops with relatively fresh exposure of Main Buntsandstein rocks.

Table 1: Samples of the P18 reservoir rocks (1 to 7b) collected at the TNO core repository in Zeist, plus those collected in the Northern Eiffel (16E and 17E). *) Suffix 'a' indicates the samples is taken perpendicular to the sedimentary layering; 'b' indicates the samples is taken parallel to the sedimentary layering. **) Only the percentages printed in bold were obtained through XRD. Others were estimated from thin section analysis. HAR = Hardegsen fm; DET = Detfurth fm; VOL = Volpriehausen fm; Qtz = Quartz; Fsp = Feldspar

Sample*	Well	Depth Interval (m)	Porosity (%)	Composition (%)**				
				Qtz	Fsp	Carbonates	Phyllosill.	Other
1a	P18-02-A01	3644.33--> 3644.52 (DET)	15	75	7.5	10		7.5
1b			12	70	7.5	15		7.5
2a	P18-02-A01	3640.50--> 3640.61 (DET)	12	84	13	3		
2b			10					
3a	P18-02-A01	3626.22--> 3626.38 (DET)	12	76	12		8	
3b			10					
4b	P18-02	3442.53--> 3442.74 (VOL)	5	65	5	10	15	5
5b	P18-02	3436.00--> 3436.36 (VOL)	8	65	16	19		
6b	P18-02	3295.00--> 3295.35 (HAR)	10	75-80	5	10 - 15		5
7b	P18-02	3287.00--> 3287.32 (HAR)	25	96		4		
16E	Sampled in the Main Buntsandstein of the Northern Eiffel		20	65	12.5		15	7.5
17E			25	80	12.5			7.5

In broad terms, the samples collected are considered to be representative of the Main Bunter sandstone. They consist of aeolian and fluviatile quartz-dominated sandstones, with considerable variation in grain size and porosity.

3.4.2.1 Composition

Alongside optical (petrographic) analysis, X-ray diffraction (XRD) analysis was carried out on representative sample fractions to quantify their composition (Table 1). Because the samples had to be crushed for XRD we could not make a distinction between the compositions parallel and perpendicular to the sedimentary layering. We have not yet completed XRD on all of the samples, and hence for now we rely on optical microscopy to estimate mineral abundances of samples 1a&b, 4b, 6b, 16E and 17E.

All samples were dominated by quartz, with contents ranging from 65% for sample 16E to 96% for sample 7b. Feldspars (i.e. orthoclase, microcline, anorthite etc.) were found in all samples, except for sample 7b, with an abundance ranging from 5% in sample 4b to 16% in sample 5b. For most P18 reservoir samples (1a&b, 4b, 5b and 6b), carbonate minerals (e.g. calcite, dolomite, ankerite) were found to be an important component, with quantities ranging from 3% to 19%.

Finally, phyllosillicate minerals (mica's, clay etc.) were found in significant proportions in some of the samples, i.e. 8% and 15% in P18 reservoir samples 3a&b and 4b, and 15% in Eiffel sample 16E.

It is important to note that the results for the Eiffel samples (16E and 17E) do not show any carbonate content, in contrast with (most) P18 reservoir rock samples. This is likely due to weathering processes, or otherwise due to lateral variation in depositional environment within the Bunter sandstone formation, e.g. aeolian vs. fluviatile deposition. Finally, the compositional variation between samples cored parallel and perpendicular to the sedimentary layering, i.e. samples 'a' vs. 'b', is minimal on the scale of our samples (Table 1).

3.4.2.2 Microstructure

Optical microscopy on polished thin sections pointed out that all samples have sub- to well-rounded grain shapes with grain sizes ranging from (very) fine to medium, i.e. from ~80 to ~500 µm. The samples have a moderately to well sorted texture (Fig 9a,d), sometimes associated with a layering that is expressed by grain size variations (Fig. 9a). Microcrystalline carbonate aggregates are often present as cement in pores between clastic grains in the P18 samples (Fig. 9b). The porosity, estimated using the linear intercept technique, ranged from 5 to 25% for both the P18 reservoir and Eiffel samples (Table 1; Fig. 9). Grain indentation structures (Fig. 9c) and local overgrowth textures point to a diagenetic history involving pressure solution compaction.

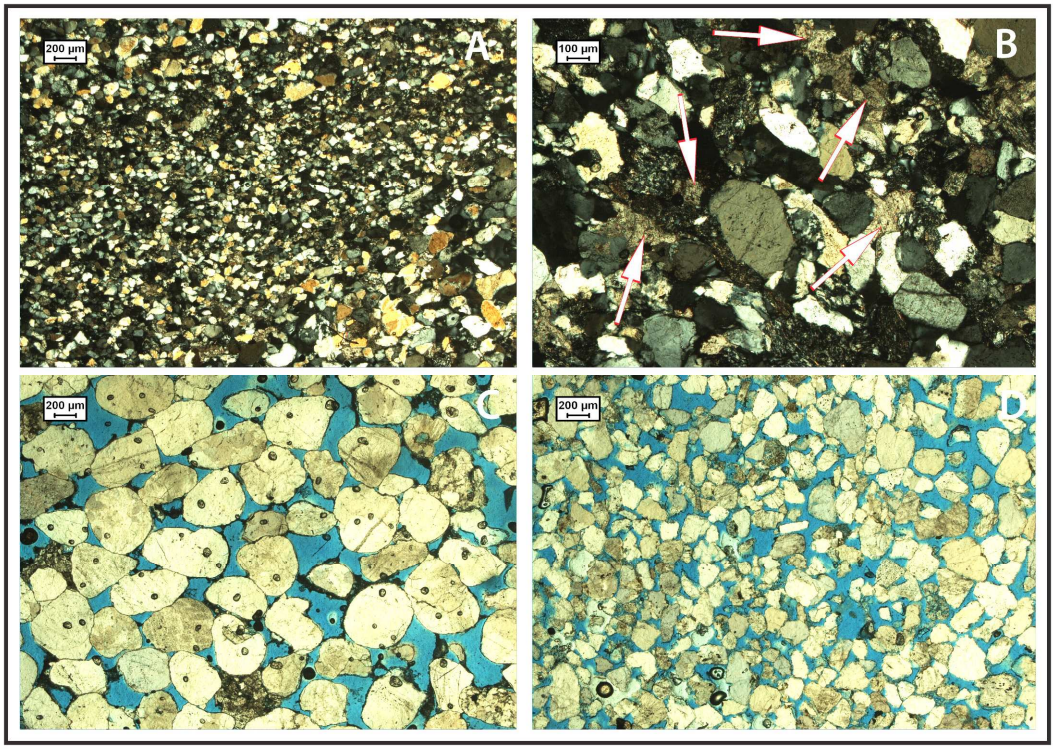

Fig. 9: Micrographs of selected samples. Note the scale bars at the top left of each photo. A: Bands of different grain size (P18 reservoir sample 1b, XPL). B: Carbonate cement, indicated by arrows, wedged between quartz grains (P18 reservoir sample 5b, XPL). C: Grain indentation structures. Note the high porosity (P18 reservoir sample 7b, PPL). D: Predominately quartz grains and a high porosity (Eiffel sample 17E, PPL).

3.4.3 Permeability measurements

Permeability data on the P18 reservoir rock samples was initially published by Amoco Petroleum Company in so-called Core Analysis Reports (CAR). These reports are publicly available at the 'NL Oil & Gas portaal' (http://www.nlog.nl/nl/home/NLOGPortal.html). However, the permeabilities listed in these reports were not measured both parallel and perpendicular to the sedimentary layering. Therefore, for this study, we prepared P18 reservoir samples 1a&b to 5b for new permeability measurements. The permeability of P18 reservoir samples 6b and 7b were taken from the CAR because their porosity is very high (Table 1, Fig. 9c) and directional dependency of the permeability of these isotropic looking samples is assumed negligible. Thus, samples 1a&b to 5b were cut and polished to obtain cylindrical samples of ~25 mm in diameter, and sample lengths varying from 15 to 25 mm. The Eiffel samples (16E and 17E) appeared too weak for this treatment; upon sawing they disintegrated. Hence we could not yet measure the permeability of those samples.

Permeability measurements were carried out using (quasi)-constant-head, steady-state permeametry and Argon transient step permeametry. For a thorough description of these methods, see Peach (1991).

3.4.3.1 Methodology

Constant-head, steady-state permeametry entails measurement of volumetric flow-through rate under a constant fluid pressure gradient, assuming no interaction between the fluid and the sample. We used demineralised, degassed water as flow medium and held the pressure gradient constant by using a relatively large upstream water reservoir that made height changes in the water column negligible (Fig. 10). Upon sample preparation, the sample was submerged in demineralised water and placed under a vacuum for several minutes. Repressurization by atmospheric pressure led to saturation of the sample with water. The sample was then jacketed with a rubber sleeve, and mounted into a pressure vessel that was pressurized with 1 MPa Argon gas to prevent leakage between the sample and the rubber sleeve. The flow rate was determined by measuring the volumetric change as a function of time. These were measured with a pipette, calibrated to 0.001 ml, and a stopwatch, respectively. Prior to measurement, the entire system was subject to a vacuum for ~20 minutes to extract unwanted (air) bubbles that could block fluid flow through sample pores.

Argon transient step permeametry entails measurement of the pressure difference decay due to flow-through following a sudden application of a pressure step, in this case applied using Argon gas as the pressure medium. Prior to measurement, the sample was jacketed with a rubber sleeve and mounted into a pressure vessel. A confining pressure of 2 MPa was applied to prevent leakage between the sample and the rubber sleeve. After connecting the vessel to the Argon Permeability apparatus (Fig. 10a), the system of tubing plus sample was evacuated to remove air using a vacuum pump. An Argon gas pressure of 1.6 MPa was then applied, at which the sample was allowed to equilibrate for several minutes. After equilibration, a sudden pressure step of ~ 0.2 MPa was applied, while the differential pressure vs. time history was being recorded by a data logging program (READ30). A second program (TRANSTEPAR) was used to calculate the permeability from this data (see Peach (1991) for more detailed discussion on the Argon transient step method).

Fig. 10: Photos of (A) the set-up used for (quasi)-constant-head, steady-state H_2O flow-through permeametry and (B) the Argon permeability apparatus, used for the transient step method. Both methods are applied to determine the permeability of P18 reservoir- and Eiffel samples of Main Bunter sandstone rocks. The steady state flow-through measurements were performed at different head lengths to confirm reproducibility of the dataset. Head lengths were varied from 0.2 to 2.2 m, corresponding to pressure gradients of ~2 to ~20 kPa. Similarly, for the transient step measurements we varied the mean upstream/ downstream pressure between 1.5, 1 and 0.5 MPa, keeping the (initial) differential pressure at 0.2 MPa.

3.4.3.2 Permeability data

Table 2 shows the data obtained from permeability (κ) measurements done on samples 1a&b to 5b, plus those obtained from the Core Analysis Report for samples 6b and 7b. The permeability of samples 6b and 7b is very high, in the order of 10^{-14} m^2 and 10^{-12} m^2 respectively, as was expected from thin section analysis (Table 1 and Fig. 9). For samples 1a&b to 5b, the permeability determined at each different head or mean pressure yielded a 'best range', for each method. However, the permeability values of samples 2b and 3a determined with the constant head flow-through method differ rather a lot. We expect that in some measurements air bubbles may have blocked pore throats within sample, and hence the measurements yield an apparent permeability that is lower than the factual value. Therefore, for samples 2b and 3a, we assumed the highest determined value to be the best representative value (Table 2). Similarly, for sample 3a, the permeability calculated for the highest mean pressure (1.5 MPa) of the transient step method exhibits an anomalous high value (Table 2). We assumed this to represent either a leak, or an opened crack, and it is therefore not taken into account for the best range value.

For the constant-head H_2O flow-through measurements, we found that the permeability of the P18 reservoir rocks ranges from 7.4×10^{-18} m^2 for sample 2a to 2.0×10^{-16} m^2 for sample 2b. The spread in the dataset, e.g. for sample 5b, indicates that the data obtained using this method was rather hard to reproduce. In general, for the Argon transient step measurements we found higher permeabilities, with values ranging from 1.1×10^{-15} m^2 for sample 2a to 6.1×10^{-17} m^2 for sample 4b. Except for sample 3a we found a value that was an order of magnitude lower than that found with the flow-through method, and for sample 4b both measurements agree fairly well (Table 2).

3.4.3.3 Discussion

The permeability data pointed out that the permeability values calculated from the steady state flow-through measurements are in general about 1 order of magnitude lower than those obtained from the Argon transient step method (Table 2). Although we cannot yet be certain, it seems likely that the H2O flow-through measurements have indeed suffered from a large uncertainty that is introduced by unwanted trapped air bubbles, a problem which appeared difficult to control (though for sample 3a we found a permeability that is an order of magnitude higher than that measured using the transient step method). Our Argon measurements were checked against a permeability standard and found to be reliable. Most of the samples therefore have a permeability of ~10^{-15} - 10^{-16} m2.

3.4.4 Fluid-rock reaction experiments

To investigate reaction in the CO_2 – reservoir rock – pore fluid system, at in-situ conditions, we have performed batch experiments on crushed sandstone samples from P18 (samples 5b and 7b) and from the Eiffel (sample 17E) (Table 1) under hydrothermal conditions in the presence of supercritical CO_2 and reservoir saline water. A key aim here is to compare results with geochemical model predictions, i.e. to calibrate, test and refine such models. Experiments were performed at temperatures of 120 - 130℃ and total pressures of 34-36 MPa. Even under relatively high pressure and temperature the kinetics of mineral trapping reactions is very slow (Hangx and Spiers, 2009). Therefore we aimed to increase reaction rates to more practical laboratory time scales by crushing our samples to an order of 1 µm using an automated agate disk miller. In this way we maintained the chemical analogy with in-situ P18 reservoir rocks. Finally, as pore-fluid saline water we used a solution of 2M NaCl + 0.2M $CaCl_2$ + 0.04M $MgCl_2$, thus representing realistic reservoir saline water like that present in the P18 field (Bert de Wijn - Wintershall, personal communication).

Table 2: Permeability data on unreacted cylinders of P18 reservoir rock (Table 1). Data for samples 6b and 7b are taken from the Core Analysis Report (CAR). Note that the Argon transient step measurements are the most reliable, as those made using water (the constant-head, steady-state method) were likely subject to effects of trapped air bubbles forming in the samples

Sample	Constant-head H2O flow-through			Argon transient step			CAR κ (m^2)
	Head (m)	κ (m2)	Range κ (m2)	Mean P (MPa)	κ (m2)	Range κ (m2)	
1a	2.2	$1{,}8 \cdot 10^{-17}$	$1.8 – 5.0 \cdot 10^{-17}$	1.5	$7.2 \cdot 10^{-16}$	$3.4 – 7.2 \cdot 10^{-16}$	-
	1.7	$2.2 \cdot 10^{-17}$		1	$3.6 \cdot 10^{-16}$		
	1.4	$2.7 \cdot 10^{-17}$		0.5	$3.4 \cdot 10^{-16}$		
	0.2	$5.0 \cdot 10^{-17}$					
1b	2.2	$4.8 \cdot 10^{-17}$	$4.8 – 6.5 \cdot 10^{-17}$	1.5	$1.7 \cdot 10^{-15}$	$1.7 – 2.0 \cdot 10^{-15}$	
	1.7	$5.5 \cdot 10^{-17}$		1	$2.0 \cdot 10^{-15}$		
	1.4	$6.5 \cdot 10^{-17}$		0.5	$1.9 \cdot 10^{-15}$		
	0.3	$5.2 \cdot 10^{-17}$					
2a	2.2	$7.4 \cdot 10^{-18}$	$7.4 – 8.8 \cdot 10^{-18}$	1.5	$1.8 \cdot 10^{-16}$	$1.1 – 1.8 \cdot 10^{-15}$	-
	1.7	$8.1 \cdot 10^{-18}$		1	$1.1 \cdot 10^{-16}$		
	1.4	$8.8 \cdot 10^{-18}$		0.5	$1.1 \cdot 10^{-16}$		
2b	2.2	$2.8 \cdot 10^{-17}$	$2.0 \cdot 10^{-16}$	1.5	$2.1 \cdot 10^{-15}$	$2.1 – 5.0 \cdot 10^{-15}$	
	1.7	$3.4 \cdot 10^{-17}$		1	$3.9 \cdot 10^{-15}$		
	1.4	$5.2 \cdot 10^{-17}$		0.5	$5.0 \cdot 10^{-15}$		
	0.2	$2.0 \cdot 10^{-16}$					
3a	2.2	$2.7 \cdot 10^{-17}$	$3.6 \cdot 10^{-16}$	1.5	$1.5 \cdot 10^{-16}$	$3.6 \cdot 10^{-17}$	-
	1.8	$2.5 \cdot 10^{-17}$		1	$3.6 \cdot 10^{-17}$		
	1.4	$2.9 \cdot 10^{-17}$		0.5	$3.6 \cdot 10^{-17}$		
	0.2	$3.6 \cdot 10^{-16}$					
3b	2.2	$2.3 \cdot 10^{-17}$	$2.3 – 4.4 \cdot 10^{-17}$	1.5	$4.6 \cdot 10^{-16}$	$1.6 – 4.6 \cdot 10^{-16}$	
	1.7	$2.4 \cdot 10^{-17}$		1	$1.7 \cdot 10^{-16}$		
	1.4	$4.4 \cdot 10^{-17}$		0.5	$1.6 \cdot 10^{-16}$		
4b	2.2	$2.7 \cdot 10^{-17}$	$2.7 – 4.4 \cdot 10^{-17}$	1.5	$6.1 \cdot 10^{-17}$	$2.7 – 6.1 \cdot 10^{-17}$	-
	1.7	$2.9 \cdot 10^{-17}$		1	$2.7 \cdot 10^{-17}$		
	1.4	$4.4 \cdot 10^{-17}$		0.5	$3.0 \cdot 10^{-17}$		
5b	2.2	$3.2 \cdot 10^{-17}$	$3.2 – 9.0 \cdot 10^{-17}$	1.5	$6.8 \cdot 10^{-16}$	$6.2 – 6.8 \cdot 10^{-16}$	-
	1.7	$3.4 \cdot 10^{-17}$		1	$6.2 \cdot 10^{-16}$		
	1.4	$4.2 \cdot 10^{-17}$		0.5	$6.3 \cdot 10^{-16}$		
	0.2	$9.0 \cdot 10^{-17}$					
6b							$1.4 \cdot 10^{-14}$
7b							$3.0 \cdot 10^{-12}$

3.4.4.1 Experimental method

The experiments were performed using a cold-seal pressure vessel, with an internal Monel K-500 reaction vessel (Fig. 11). In order to prevent Ni-contamination from the reaction vessel it was capped with a 2 µm Titanium grade 2 frit, and isolated from the reactive contents with a Teflon liner. For a thorough description of the experimental set-up, see Hangx and Spiers (2009), whose experimental methodology we followed, and tried to improve.

In these experiments, which are ongoing, for each run the reaction vessel is filled with 0.1 – 0.2 g of crushed sample material. In order to prevent desiccation of the sample due to evaporation of water into the supercritical CO_2 we add excess saline water to completely submerge the sample, i.e. typically 0.5 to 1 ml. The reaction vessel is then mounted into the cold-seal pressure vessel using a stainless steel rod (Fig. 11a), and pressurized to an initial (total) pressure of ~17-18 MPa using a separated Argon cylinder buffered CO_2 supply. An externally applied furnace (Fig. 11b) increases the internal temperature to ~120 - 130℃, and consequently, within roughly 1 hour, the internal pressure has risen to 34 – 36 MPa.

The experiments are planned to run for 3, 9 and 27 days duration. They are terminated by rapidly depressurizing (< 1 min) the system, prior to cooling, which causes saline water to be expelled from the system and preventing re-dissolution of any precipitated secondary phases. After extraction, the samples are analyzed by means of Scanning Electron Microscopy (SEM), Thermogravimetric Analysis (TGA), Fourier Transform Infrared spectroscopy (FTIR) and X-ray Diffraction analysis (XRD). Comparing these analytical results with those obtained from unreacted crushed material will yield an indication of the identity and, if sufficient, amounts of products formed.

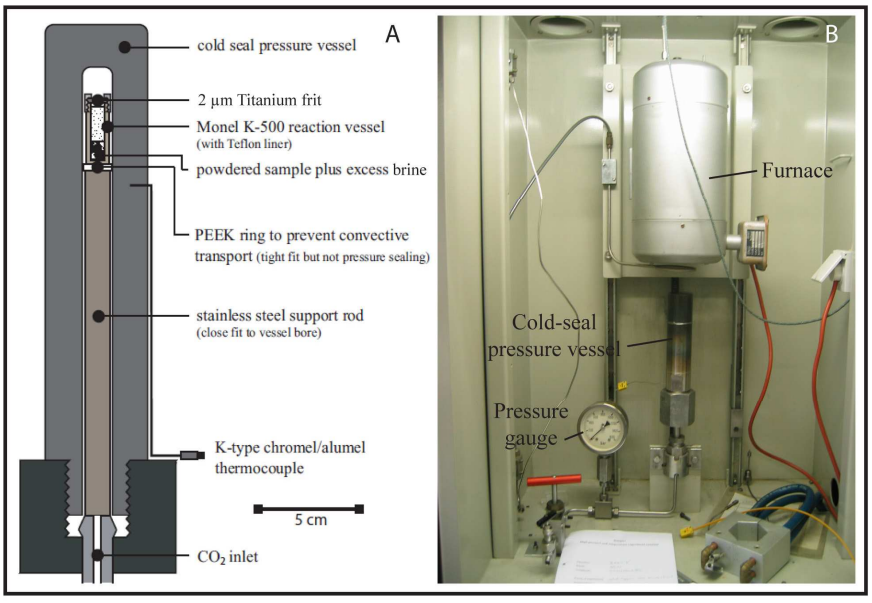

Fig. 11: A) Schematic illustration of the cold-seal pressure vessel set-up, used for reaction experiments on P18 reservoir (sample 5b and 7b) and Eiffel samples (sample 17E) of the Main Bunter sandstone formation (Table 1). Modified from Hangx and Spiers (2009). B). Photo of the experimental set-up.

3.4.4.2 Progress and further work

So far, we have conducted two rounds of experiments, one round of three days and another round of 27 days duration (Table 3). Upon removal from the reaction vessel, the samples were still wet, with crushed sample material suspended in the pore fluid. The inner surface of the titanium frit was in all cases covered with a thin layer of sample material, indicating that at least some of the fluid was expelled from the reaction vessel, probably during depressurization. After extraction, the samples were put in an oven and dried at 50℃. Detailed analysis of the samples is in progress and no data are yet available.

These experiments are presently being extended to durations of 9 days, but also to durations of several months to allow for longer reaction times. In order to accelerate reaction rates, we further intend to explore the use of finer grain sizes (≤ 1 µm) and higher temperatures. Note that the anticipated results will yield qualitative insights on the extent and nature of reactions occurring in the system supercritical CO_2 – sandstone – saline water, under in-situ conditions. Little useful kinetic data or solution chemistry data can be obtained. Nonetheless, out results will provide useful information for validating model predictions regarding long term reaction products and for constructing, calibrating and testing models predicting the effect of reaction on microstructure, porosity and transport properties (cf. Hangx and Spiers, 2009).

Table 3: Reaction experiments on P18 reservoir (samples 5b and 7b) and Eiffel samples (sample 17E) completed thus far. Experiments 17Ereact1 and 7Breact1 were conducted at a lower pressure. Experiment 17Ereact2 suffered from an unexpected leak, so that the pressure dropped ~15 MPa over the course of the experiment. *) The pore fluid used was a solution of 2M NaCl; 0.2M $CaCl_2$.

Experiments (P ≈ 35 MPa T ≈ 120℃)	17E	7b	5b
~3 days	17Ereact1* (P = 19.5 MPa)	7Breact1* (P = 24 MPa)	5Breact1*
~27 days	17Ereact2 (dP/dt < 0)	7Breact2	5Breact2

3.4.5 Conclusions and next steps

Representative samples of Bunter sandstone reservoir rocks from the P18 gas field in the North Sea, presently considered for CO_2 sequestration, were obtained from the TNO core repository in Zeist. In addition, we conducted a field excursion to the Northern Eiffel of Western Germany to collect more samples of a similar facies and composition.

X-ray diffraction and thin section analysis showed that all samples are dominated by quartz (65%-96%), with minor amounts of feldspar (5%–16%), carbonates (3%-19%) and/ or phyllosillicates (8%-15%). Carbonate minerals were not found in the samples retrieved from the Northern Eiffel, probably partly due to weathering processes, or perhaps due to lateral facies variation. Microstructural investigation using optical microscopy showed that the samples studied have a comparable rock texture, with similar sub- to well-rounded grain shapes and a porosity ranging from 5% to 25%. There is significant vertical, and presumably horizontal, variation in chemistry and porosity within the P18 reservoir.

Permeability measurements indicate that the permeability of the P18 reservoir rocks is mostly in the order of 10^{-15} to 10^{-16} m2. Lower values were obtained using the (quasi)-constant-head, steady-state H_2O flow-through method, but these are probably erroneous due to trapped air bubbles blocking fluid flow through. A third method, i.e. steady state Argon flow-through permeametry, will be employed shortly to check the dataset.

Finally, reaction experiments on the system CO_2 – reservoir rock – saline water have been carried out using a cold-seal experimental set-up under in-situ P18 reservoir conditions (Fig. 3). Experiments were performed on crushed sample material (grain size ~1 µm), and were, so far, run for 3 days and 27 days. The reacted samples from these experiments are currently being analyzed for comparison of their composition with the unreacted crushed sample material. In the (near) future, the experiments will be extended to longer durations (several months), while finer grain sizes and higher temperatures will also be explored. In future, the results will provide a means of testing and calibrating long term model predictions, and will form a basis for modelling porosity and permeability evolution.

Acknowledgements

TNO Bouw & Ondergrond in Utrecht and the TNO core repository in Zeist are kindly acknowledged for their help in retrieving the appropriate P18 reservoir rock samples. Further, we'd like to thank Peter van Krieken and Gert Kastelein for their assistance in performing the lab experiments, and Roderick van de Kroeff for his study of the thin sections.

3.5 Reservoir behaviour

3.5.1 Enhance mass-transfer simulations

The aim of this meso-scale simulation study is to examine whether (1) small scale (reservoir) heterogeneities and (2) geochemical reactions influence the long-term mass transfer of CO_2 by natural convection in a reservoir. Meso-scale is loosely defined as being between 10 and 1000 cm in size: larger than the samples of experiments, but smaller than geological heterogeneities. Currently available software packages do not properly capture the process of (natural) convection induced by CO_2 dissolution in combination with the occurrence of geochemical reactions. Therefore, an in-house simulator is in development at DUT: preliminary results are presented here.

The (2D) domain has a width and height of 1 m and is subdivided by 101×101 grid cells. The numerical modelling is done using in-house MATLAB^{TM} code. The homogeneous medium has an initial permeability of $1.0 \cdot 10^{-12}$ m^2 and a porosity of 0.4. The heterogeneous medium is mimicked by stochastically assigning a porosity value for each grid block using the Sequential Gaussian Simulation (SGSIM) method developed by GSLib. The permeabilities is calculated from these porosity values by a Kozeny-Carman type of equation. The porosity, and thus also permeability, changing processes of dissolution and precipitation of the porous medium, consisting of pure calcite, is incorporated in the simulation when considering the occurrence of geochemical reactions.

Fig. 12 shows concentration maps of the dissolved CO_2 after a simulation time of 80 years for (a) homogenous porous medium without the occurrence of geochemical reactions, (b) heterogeneous porous medium without the occurrence of geochemical reactions and (c) homogeneous porous medium with the occurrence of geochemical reactions. All three figures show the characteristic fingering of (natural) convection (Farajzadeh, 2009) induced by the increase in water density due to the dissolution of CO_2.

The heterogeneity of the porous medium, compared to homogeneous medium (Fig. 12(a) vs. Fig. 12(b)), results in more irregular boundaries, less fingers and deeper penetration. This demonstrates that small scale heterogeneities influence the mass transfer rate of CO_2 into the saline water.

The incorporation of geochemical reactions in the simulations using homogeneous porous medium leads to fewer fingers with deeper penetration (Fig. 12c *vs.* Fig. 12 a). This is because geochemical reactions result in a density increase of the water due to its increased ionic concentration. This increased density enhances (natural) convection leading to deeper but fewer fingers. Thus, the incorporation of geochemical reactions is crucial for adequate description of the mass transfer of CO_2 into the saline water.

Future work will focus on the implementation of the implications of these small scale effects on field scale simulations.

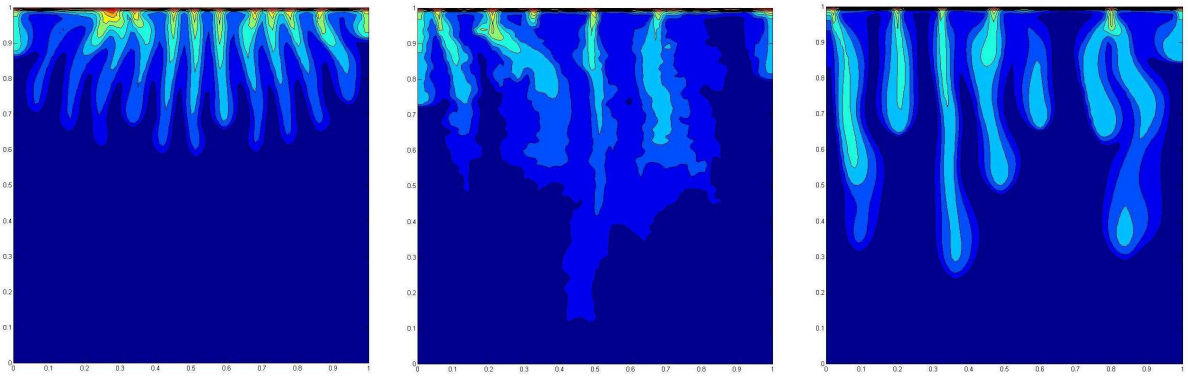

(a) (b) (c)

Fig. 12: Simulation of concentration of dissolved CO_2 in a 1 X 1 m block obtained, 80 years after injection (Rayleigh number = 10000): (a) homogeneous porous medium without the occurrence of geochemical reactions, (b) heterogeneous porous medium without the occurrence of geochemical reactions, (c) homogenous porous medium with the occurrence of geochemical reactions. See text for description and explanation of the differences in CO_3 spreading.

3.5.2 Mineralization of CO_2 in Rotliegend sandstone

Summary of the article by Ranganathan et al. (2010), presented at the GHGT-10.

The objective of this study is to investigate whether the mineralizations are important when sequestering CO_2 in Rotliegend sandstone. Rotliegend sandstone is selected as this formation is being considered for sequestration of carbon dioxide in the Netherlands. The importance of mineralization is investigated by means of a CMG-GEM simulation study. CMG-GEM is a commercial simulator often used for the simulation of CO_2 sequestration in aquifers with geochemical reactions. The article (Ranganathan et al., 2010) contains addition information, including a sensitivity study of key parameters (porosity, permeability, residual gas saturation and geochemical kinetic coefficients).

The formation is homogeneous (porosity of 0.18 and permeability of 200 mD) and is 15 km×15 km×50 m large. The mineral and formation water composition are taken from Wilkinson *et al*. (2009), who reported these data for the Rotliegend sandstone formation in the UK. The water and gas relative permeability curves are obtained using the Brooks-Corey equation (Bear, 1972); the capillary pressure curve is computed using the van Genuchten (1980) correlation; the solubility of CO_2 in brine is modelled using a Henry's law correlation (Li and Nghiem, 1986); the PVT behaviour of the CO_2- saline water mixture is described using the Peng-Robinson equation of state (Peng and Robinson, 1976). Furthermore, the geochemical reactions and their kinetic parameters are taken from Nghiem *et al*. (2004). The grid of the formation consists out of ten layers by grid blocks of 300 m x 300m x 5m. The injection well is located at the centre of the field and CO_2 is injected over the length of the well using a constant rate of 1.0MTon /year for the period of 16 years. The boundaries of the field are considered open and thus specified at constant pressure. The simulation is carried out over a period of 10,000 years (including the 16 years of injection).

Fig. 13 shows the 3D distribution of the CO_2, 5000 years after start of injection, in the gas phase and dissolved in the saline water (aqueous solution). Fig. 14 is similar, but for 10.000 years after start of injection. The injected CO_2 initially migrates towards the top of the reservoir due to gravity

segregation. Subsequently, CO_2 spreads laterally and dissolves in the formation water. The dissolution of CO_2 results in an increase of the density of the brine, which causes natural convection induced fingering similar to that observed in the meso-scale simulations (see Section 3.5.1).

Fig. 15 displays the distribution of CO_2 trapped by the various trapping mechanisms (mobility, solubility and mineral trapping) as function of time: most of the CO_2 is stored by solubility and mobility trapping in the Rotliegend sandstone formation; however, mineral trapping is not negligible and the incorporation of mineralizations is crucial for adequate description of the reservoir behaviour.

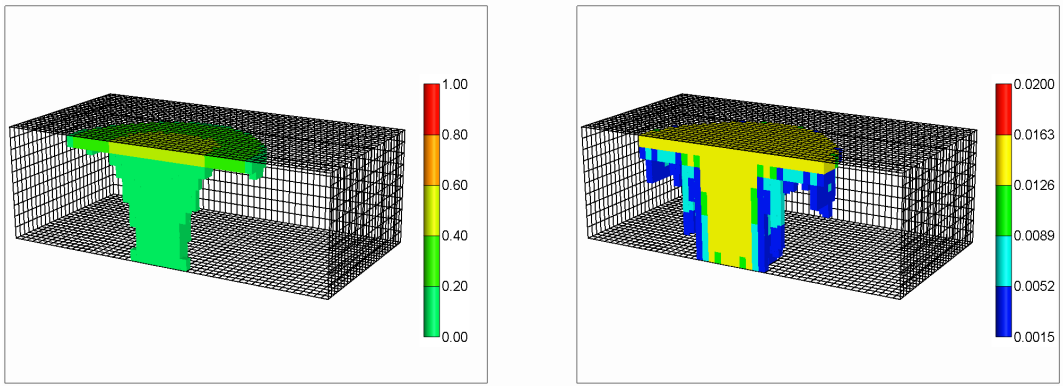

Fig. 13: Spatial distribution of (a) CO_2 gas saturation and (b) CO2 concentration dissolved in aqueous phase after simulation time of 5000 years.

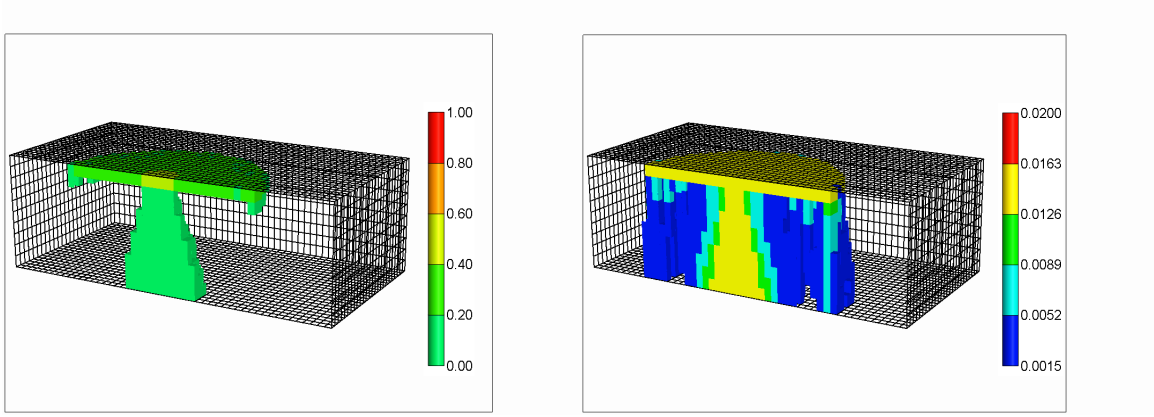

Fig. 14: Spatial distribution of (a) CO_2 gas saturation and (b) CO2 concentration dissolved in aqueous phase after simulation time of 10,000 years.

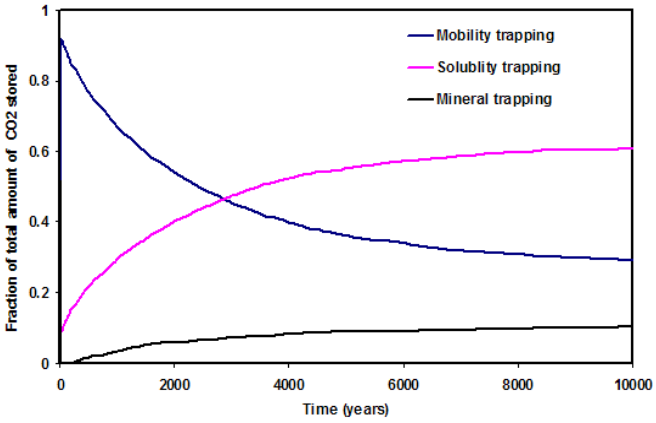

Fig. 15: Distribution of trapped CO2 into mineral, solubility and mobility trapping as function of time for the Rotliegend Formation (total simulation time = 10,000 years).

3.5.3 Reactive transport modelling in TOUGHREACT

3.5.3.1 Introduction

Reactive transport modelling is a tool that can be used to account for a combination of water and gas flow and geochemical reactions. Predictions of the short- and long-term geochemical response of a reservoir and caprock can be made as a result of, for example, CO_2 injection. This is important as dissolution of CO_2 in the formation water will lead to a decrease in pH, which will then be buffered by mineral dissolution and precipitation, possibly followed by transport of the reaction products throughout the reservoir. This chapter describes the setup of a generic reactive transport model using *TOUGHREACT* and the Petrasim interface. Such a generic model will be used as a starting point in discussion with operators about a specific site.

3.5.3.2 Generic setup of reactive transport model in TOUGHREACT

A few model grids can be used to describe potential storage reservoir. Many grid cells are preferred for an accurate description, as well as taking into account the exact the geological model. In practice this is quite complex and often more simple models are used as a starting point, taking into account the geological layers and sufficient accuracy. A 2D window from a radial grid, as shown in Fig. 16, is an efficient alternative for a rectangular 3D grid.

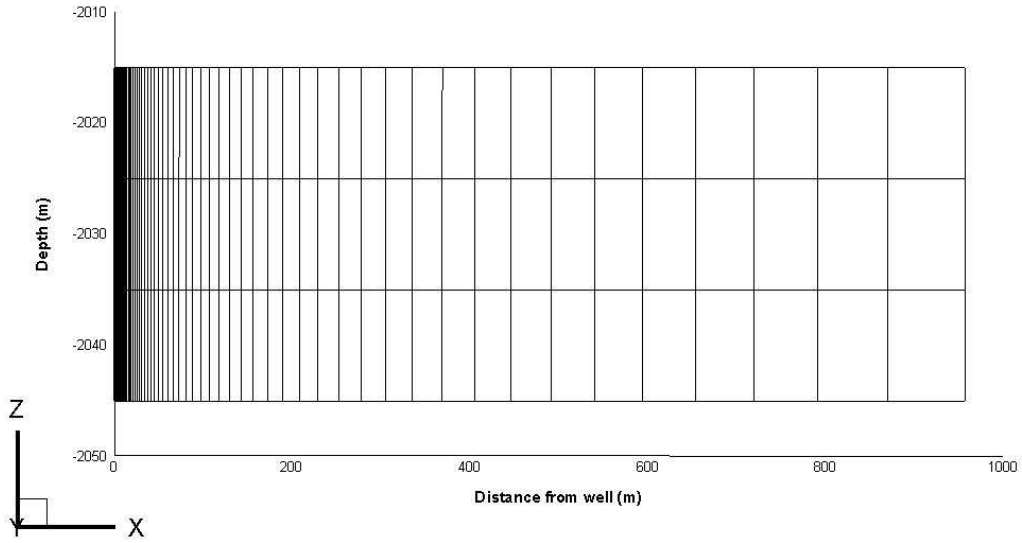

Fig. 16 : 2D window (cell-centered) of a radial model containing four layers of 100 grid cells. Near-well effects are taken into account by defining fine grid cells close to the well

Fig. 16 shows that very fine grid cells are present close to the well, thereby accounting for near-well effects. The grid cell sizes in the X direction range from 7.0×10^{-3} m to 91.0 m. The reservoir is set-up in such a way that it has a sufficiently large porosity (i.e. 20%) and permeability (100 mD), at a depth of 2010 m, and a connate water content of 15 %. This liquid saturation is too low for water flow (relative permeability of 0) and accounts for full gas flow (relative permeability of 1.0). The temperature is 70°C and the initial pressure is 30.0 bars. The specified initial mineralogy is equal for all grid cells, thereby accounting for one uniform geological layer. The mineralogical composition if very basic, consisting of quartz (72 vol%), albite (4 vol%), and K-feldspar (4 vol%).

Six secondary precipitating minerals were allowed: dawsonite, diaspore, kaolinite, muscovite, pyrophyllite, and paragonite. The brine mass fraction is 0.07 and the formation water composition is computed from the initial mineralogy (disabling secondary mineral precipitation).

Fig. 17 shows the gas saturation as a function of the distance to the well, which initially is 0.85 throughout the reservoir. Water evaporates in the dry CO_2 gas stream during injection, leading to a dry-out area in the vicinity of the well-bore. After shut-in of the well, only marginal changes are computed and thus the effect describes a short term process. The results show a drying-out front that increases over time, with a final radius of 96.8 m. This radius is a direct function of the total amount of CO_2 injected, porosity, initial water saturation, temperature, and (final) pressure. After a relatively small transition zone, the gas saturation is computed to remain constant ($S_g \approx 0.848$) in the remainder of the reservoir up to 1000 m away from the well. The amount of salt that precipitates in the dried out area takes up approximately 0.5% of the total pore volume, which is much less than recently computed for saline aquifers (i.e. 9.1%) by Pruess and Muller (2009). The reason for this difference is that more water and hence more salt is present in saline aquifers. At this point it can not be excluded that minor amounts of salt will lead to pore neck clogging, this should verified by future research. Clay shrinkage due to drying out could lead to geomechanical effects.

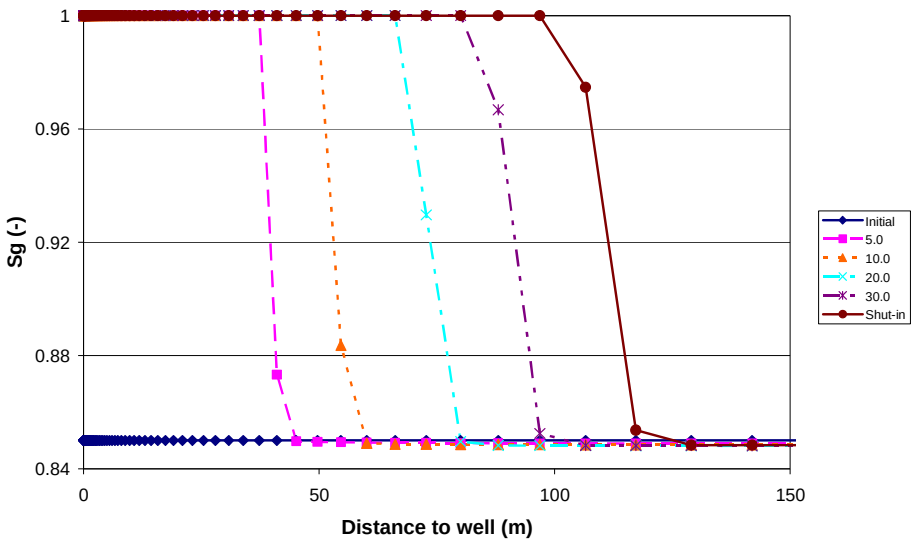

Fig. 17: Gas saturation (S_g) or drying out front as a function of the distance to the well during CO_2 injection into the reservoir after 5, 10, 20, and 30 years. After an injection period of 41.5 years the well is shut-in and the gas saturation does not change significantly. Salt precipitation occurs in the drying out area.

Mineral transformation as a function of time is shown in Fig. 18, for the area of the reservoir that is not dried out. Conversion of albite into dawsonite is predicted, but transformation of small amounts of K-feldspar into kaolinite, muscovite, and pyrophyllite also occurs. The associated porosity change as a function of time is shown in Fig. 19. The transformation of albite into dawsonite is responsible for a porosity decrease from 20% to approximately 19.0% (corresponding to a 5.0% reduction of the pore volume) after 100,000 years. This is related to the relatively low density of dawsonite of approximately 2.42 g/cm^3, compared to a density of 2.56

g/cm3 for K-feldspar. The pressure may increase due to the reduction of pore volume, assuming no effect of pressure on the geochemical reactions. The stability of dawsonite is part of an ongoing debate (Gaus, 2010), as it is not always observed in natural analogues of CO_2 storage. The results presented here do not take into account porosity reduction as a result of geomechanical compaction.

The pH of the formation water as a function of time is also given in Fig. . Shortly after injection, the pH decreases to 3.3 and is then slowly buffered to a value of 4.4. This buffering is a result of mineral dissolution and precipitation.

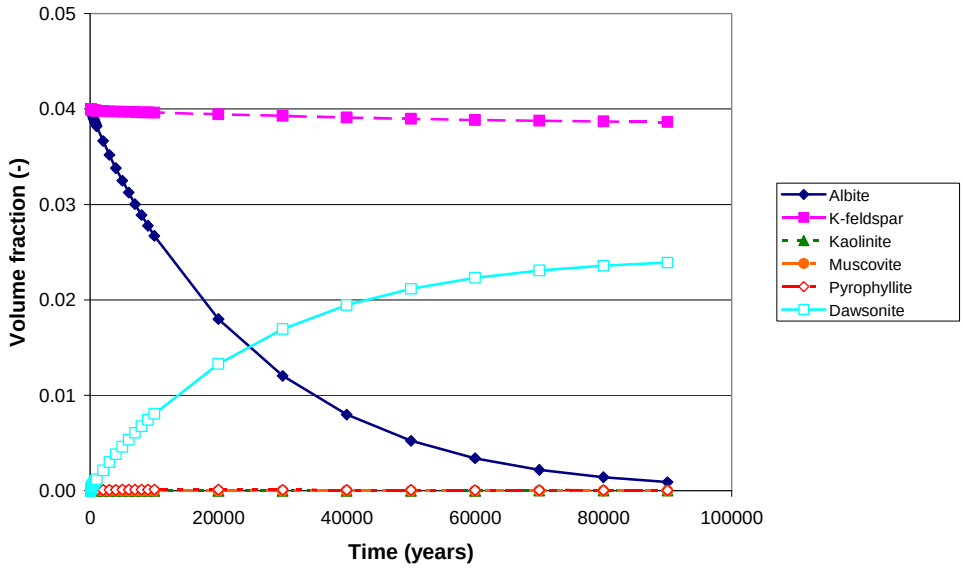

Fig. 18: Volume fractions of the minerals in the generic reservoir as a function of time, representing the reservoir area that is not dried out. The volume fraction of quartz is one order of magnitude higher and is therefore not shown.

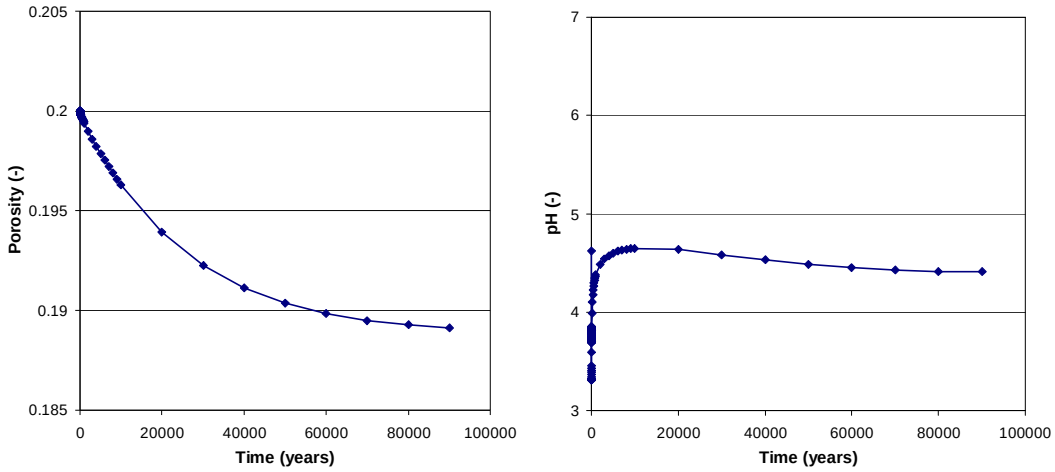

Fig. 19: The porosity (left) and the pH (right) as a function of time. The results represent the reservoir area that is not dried out.

3.5.3.3 Application to P18 site (TAQA)

Mineralogy

The generic model setup, as described in the previous section, was applied to the P18 site. The model consists of five layers, each with specific depth, thickness, porosity, permeability, and mineralogy. An overview of the all the data used is given in Table 4. Based on the permeabilities it seems likely that the Hardegsen formation will be most suitable for CO_2 injection and the Upper and Lower Dethfurth formations to a less extent. The Volpriehausen formation and the caprock have very low permeabilities and can be considered as quite impermeable.

Table 4: Overview of data used in the P18 *TOUGHREACT* model, based on the analyzed data for well P/18-3 (Cantwell, 1992). The caprock data is based on the P15 seal (Spain et al., 1991), as discussed in CATO-2 Deliverable WP3.03-D07.

	Caprock	Hardegsen	Upper Dethfurth	Lower Dethfurth	Volpriehausen
Top Zone (m)	3426	3456	3482	3532	3554
Base Zone (m)	3456	3482	3532	3554	3667
Average depth (m)	3441	3469	3507	3543	3611
Thickness (m)	30	26	50	22	113
Temperature (°C)	104	105	106	107	109
Initial P (bar)	390	392	396	399	405
Porosity (-)	2.5	11	8	8	3
Permeability (mD)	0.01	154.40	38.54	30.55	0.21
Mineral	**Volume fraction (-)**				
Albite	-	-	0.002	-	-
K-Feldspar	0.0390	0.0598	0.0646	0.0556	0.0631
Quartz	0.6269	0.8162	0.7628	0.7851	0.6088
Dolomite	0.1129	0.0371	0.0595	0.0651	0.1032
Anhydrite	0.0643	0.0022	-	-	-
Anorthite	0.0286	0.0193	0.0251	0.0225	0.0292
Clinochlore-14a	0.0074	0.0074	0.0159	0.0166	0.02
Illite	0.1002	0.0277	0.0299	0.0241	0.0827
Kaolinite	-	0.0026	0.0103	0.0069	0.0104
Smectite-Na	0.0013	0.0277	0.0299	0.0241	0.0826
Pyrite	0.0029	-	-	-	-
Siderite	0.0165	-	-	-	-

Formation water

The composition of the formation water needs to be defined before starting the computations on a reservoir scale. Here the formation water composition is computed from the reservoir mineralogy and equilibrium is assumed after 10 years, taking into account secondary mineral precipitation. An alternative approach is taking the thermodynamic equilibrium as a starting point, without secondary mineral precipitation. The disadvantage of this is that thin sections may show that specific minerals are covered by other minerals or occur as mineral inclusions, thereby (temporally) limiting their accessibility (Peters, 2009). In addition to this, the measured reservoir

mineralogy composition may not represent an equilibrium situation as slow transformation of clay minerals, for example, is still ongoing.

The most important advantage of computing the formation water, rather than using experimental measurements, is that the actual simulations will then start from a well-defined and reproducible initial situation. Experimentally measured formation water compositions will not be in equilibrium with the measured reservoir mineralogy once supplied to and modelled with geochemical software. In such cases the judgement of the user on defining the initial (equilibrium) situation may then contain subjective elements. Furthermore, downhole formation water samples are quite often not available for specific sites and very expensive to retrieve. If they are available they may contain contamination from, for example, drilling muds. Degassing of dissolved CO_2 during sampling and storing may influence the measured pH. Thoughts about the experimentally measured formation water were also brought up by others (Gaus et al., 2005; Audigane et al., 2008).
The workflow below describes computation of the formation water composition in this study:
a) Only one grid block (no flow) with the initial mineralogy is defined.
b) All the pores are completely filled with brine (cbrine = 100 g/l), defining the Na^+ and Cl^- concentrations, while the concentrations of other primary species are defined as negligibly small.
c) A background partial pressure of CO_2 is defined in addition to the temperature (T) and total pressure (P) in the reservoir.

The equilibrium formation water compositions are computed for all geological layers (besides the caprock) and the applied to the full scale mode of 100 grid cells per layer. The formation water composition is given in Table 5.

Table 5: Formation water composition, computed from the mineralogy of the four geological layers of the P18 field. The H^+ concentration is shown appears to be negative, but this is related to the

	Concentration (mol/kg water)			
	Hardegsen	**Upper Dethfurth**	**Lower Dethfurth**	**Volpriehausen**
AlO_2^-	3.23E-04	4.47E-04	4.70E-04	7.05E-04
H^+	-7.93E-03	-7.01E-03	-1.03E-02	-7.63E-03
H_2O	1.00E+00	1.00E+00	1.00E+00	1.00E+00
K^+	5.74E-08	9.42E-08	4.28E-08	1.20E-07
Na^+	1.27E+00	1.23E+00	1.27E+00	1.26E+00
SiO_2 (aq)	4.01E-03	3.16E-03	5.62E-03	3.37E-03
Cl^-	1.29E+00	1.29E+00	1.29E+00	1.29E+00
Ca^{2+}	4.36E-02	3.46E-02	1.98E-02	2.00E-02
Mg^{2+}	1.15E-07	9.14E-08	4.77E-08	5.99E-08
HCO_3^-	5.88E-03	5.83E-03	7.47E-03	6.78E-03
SO_4^{2-}	2.69E-02	1.00E-20	1.00E-20	1.00E-20

3.5.3.4 Final remarks

The results presented in this chapter show the setup of a reactive transport model, which will be applied to the P18 field case. The mineralogical data of the P18 field was evaluated and the associated formation water composition was estimated by computation. The results will be applied to a full scale model in the future, in which also other processes (such as Joule-Thomson effect) will be taken into account.

3.5.4 Near-wellbore reservoir modelling for P18

During the first CATO2 year, most of the attention has been directed towards the P18 fields of TAQA. This operator plans to inject CO_2 into the mature P18 reservoirs. The P18 compartments are deep (over 3 km depth) and quite permeable. This together with the off-shore nature of the injected and the associated cooler temperatures of the injected CO_2 means that it is essential to include thermal aspect and processes, such as the Joule-Thompson cooling, impact on induced fracturing etc. in the feasibility study.

Most current reservoir models do not allow to model thermal effects together with an description of the PVT, according to the EOS. In a project before CATOII, TNO has been successful in modeling the thermal impact of injection into the Barendrecht reservoir. As this was a NAM field, we applied the Shell reservoir model MoReS. TNO at that moment was not allowed to use the Shell model for other producers. It was therefore decided to translate the MoReS input files into those for Eclipse300 (+ thermal).After trying several approaches, spending a lot of time and after several talks with Schlumberger it was decided that the current version of Eclipse cannot model the thermal effects of CO_2 injections into a depleted (composition) gas reservoirs.

The next approach was to ask Shell Siep to make the MoReS simulator available for TNO reservoir engineers to work on reservoirs within CATOII. Shell agreed to this and allowed the use of MoReS for the P18 and P15 fields (operated by TAQA Energy B.V., and the K12-B blocks operated by GDF Suez E7P Nederland B.V. It was then decided to use the so-called pseudo as used for the Barendrecht for the P18 fields.

In other to include small-scale processes in the simulation, a radial sector model was used with very small (1.5 cm) grids directly adjacent to the injection well and much larger grids, further away from the well. The total length of the flow domain was 2 km.

Together with TAQA, a workflow was set up which included integration of the modeling efforts of TNO and the TAQA contractor Genesis. Within the framework, Genesis was responsible for modeling the transport from the on-shore CO_2 source, and the transport/behavior of CO_2 within the injection well. For various scenario's Genesis modeled the injection rate, bottom hole pressures and temperatures, which subsequently were applied as input data for the reservoir simulation as conducted by TNO.

Genesis provided the data on a number of scenarios. Two of these were subsequently modeled by TNO (Bottom Hole Temperatures of 285 K and 259 K, respectively).

A difference between the injection in Barendrecht and P18 is the temperature of the injected CO_2.and the injection rates. We controlled the modeling of the C_p of the liquid phase which was found to be reasonable. Another change was the way MORES manages the time steps of the simulation.

Fig. 20 shows the simulation results (BHT = 285 K) the temperatures around the injection well after 1 day and 1 year of injection, respectably.

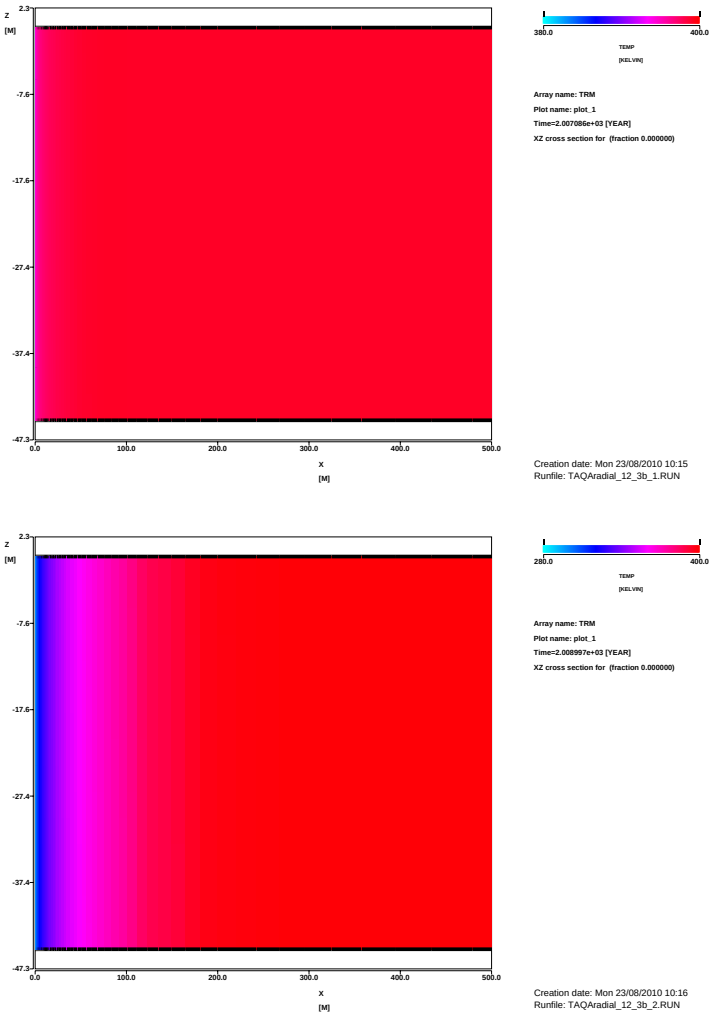

Fig. 20: Temperature profiles after 1 day and 1 year of injection, respectively.

Fig. 20 shows that temperatures, close to the injection well, drop several degrees within 1 Day. Subsequently the temperatures gradually drop further from the initial temperature of the reservoir to that of the injected fluid. After 1 year of injection a very small near well area has reached the temperature of the injected fluid. After the bottom hole has reached 80 Bars, hydrate formation may become a problem.

Outlook:

As this was the first time, we applied the pseudo-thermal approach for injection of liquid CO_2, extensive quality control has been taking place. Now this appears to be completed, we will look at the impact of fluctuations in the supply of CO_2 on the temperatures in the near-well area.

3.5.5 Effects on the near-well

3.5.5.1 Introduction

Near-well processes during injection of CO_2 in depleted gas reservoirs are complex, exert a crucial control on injectivity and, hence, need to be thoroughly understood and predicted. In this work, a numerical simulator has been set up and was used to quantify and assess the role of processes which have the potential to negatively impact well-injectivity. Modelling focused on two key processes:

- formation dry-out in the vicinity of the well causing dissolved salts to precipitate and porosity and permeability reduction
- Formation cooling due to CO_2 expansion during injection in a relatively low pressure reservoir (Joule-Thomson effect), potentially leading to freezing of the residual water and the formation of hydrates.

3.5.5.2 Methodology: Conceptual model of reservoir and sensitivity studies

Simulations were performed with the multiphase, multicomponent fluid and heat flow code TOUGH2 V2 (Pruess, 1999) in combination with the fluid property module ECO2N. This property module describes the thermodynamic and thermo-physical properties of the H_2O-NaCl-CO_2 system (Sphycher and Pruess, 2004). Dissolution of CO_2 and H_2O in the gas and brine phases, and precipitation of salt are simulated. Chemical interactions between fluids and the formation minerals have not taken into account in the present simulations. Near-well processes were studied for a sandstone reservoir with parameter values representative of a depleted gas field in the Netherlands (Tambach et al., 2009). The reservoir is assumed to be homogeneous, with no-flow boundaries representing impermeable upper and lower layers, and bounding faults. Parameter values were varied relative to the following base case settings: initial pressure and temperature 20 bars and 80℃ respectively; initial water saturation 15% and salinity 10% by weight; porosity and permeability 20% and 100 mD respectively; relative permeability parameters (Corey's model) S_{lr}= 0.15, S_{gr}=0.05. A simplified two-dimensional radial-vertical geometry (2-D R-Z) was chosen with a reservoir thickness of 20 m and radial extent of 1000 m. Injection of CO_2 is modelled to occur uniformly over the height of the reservoir. For the base case, injection lasts 2 years at an injection rate of 8 kg/s.

In the sensitivity analysis the following parameters and conditions were varied: injection rate, injection temperature, isothermal/non-isothermal simulation, accounting/ignoring capillary pressure, assuming seasonal injection scheme, and in initial water saturation. Table 1 gives an overview of the simulations.

Table 6: Overview of simulations

Run #	CO_2 injection rate (kg/s)	T_{inj} (℃)	Model	P_{cap}	Variation
1	8	80	Non-isothermal	No	**Base case**
2	8	80	Non-isothermal	Yes	Inclusion of P_{cap}
3	8	80	Isothermal	No	Isothermal simulations
4	8	35	Non-isothermal	No	T_{inj}
5	4	35	Non-isothermal	No	T_{inj} ;Q
6	16	35	Non-isothermal	No	T_{inj}; Q
7	8	35	Non-isothermal	Yes	irreducible liquid saturation Slr from 0.15 to 0.05
8	8	35	Non-isothermal	No	Seasonal injection*
9	8	35	Non-isothermal	Yes	Increase in Sw from 0.15 to 0.5

*sequential scheme of injection/shut-in periods of 3 months each

3.5.5.3 Results: Formation dry-out and solid precipitation and Joule-Thomson cooling

Fig. 21a illustrates predicted formation dry-out two years after the start of injection. Dry-out can be recognized where, due to evaporation of residual water into the CO_2 stream , gas saturation has become higher than the initial gas saturation (Sg=0.85). Results show that, for a given initial Sg, formation dry-out is relatively insensitive to the injection rate and rather sensitive to the CO_2 injection temperature. Furthermore, the width of the dry-out zone is inversely related to initial water saturation (run #9).

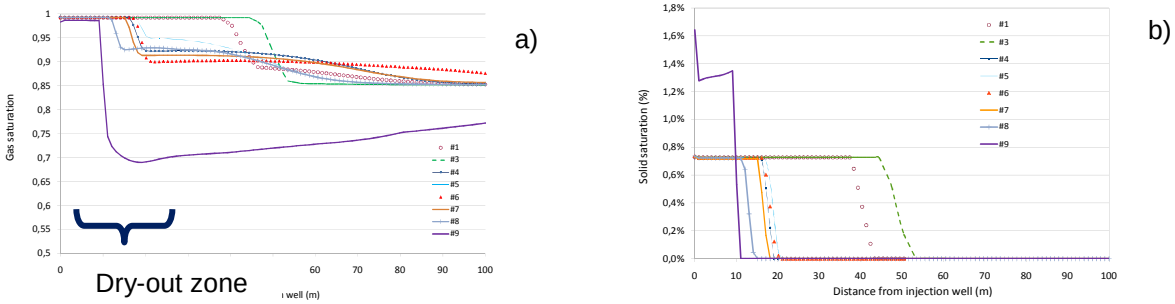

Fig. 21 a) Gas Saturation profiles and b) solid saturation profiles after 2 years of continuous injection.

Fig. 21b shows the corresponding solid saturation (fraction of pore space filled by precipitate) profiles. Solid precipitation occurs behind the dry-out front. For the choice of parameters used in the simulation, porosity reduction is less than 1% and largely scales with initial brine content and its salinity.

Fig. 22 shows the predicted cooling in the 80 ^{0}C reservoir due to the combined effects of relatively cold injection temperature (runs #4-9) and the Joule-Thomson effect. For the same amount of CO_2 injected, the extent of the cold zone that develops is approximately the same for all runs. The cold front extends deeper into the reservoir for higher initial water content (run #9). The magnitude of the (JT) temperature drop mainly depends on the injection rate. In the experiments, largest JT-cooling (appox. -17℃) is achi eved for the higher injection rate (Q=16 kg/s). JT-cooling further is slightly dependent on injection temperature (runs #1 and 4), where cooling is somewhat stronger at lower injection temperatures (for the same pressure drop). Seasonal injection (run #8), i.e. scheme of injection/shut-in periods does not appear to cause markedly different cooling patterns.

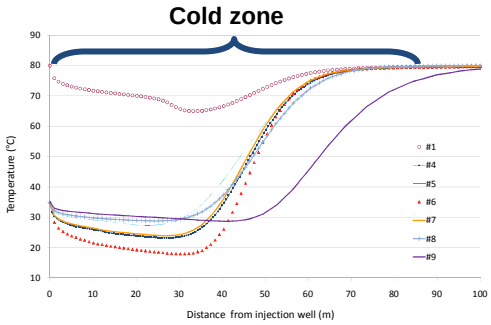

Fig. 22: Evolution of temperature profiles in the reservoir. The total amount of CO_2 injected is the same for all cases.

In addition to the above factors, JT-cooling is also affected by reservoir permeability. Fig. 23 shows the temperature distributions after 1 year of injection assuming homogeneous permeability (23a) and when permeability varies in the vertical (23b). For the employed constant injection rate, cooling varies among the layers, with larger cooling where permeability is are lower. In lower permeability zones the generated ΔP is larger and hence the associated JT effect.

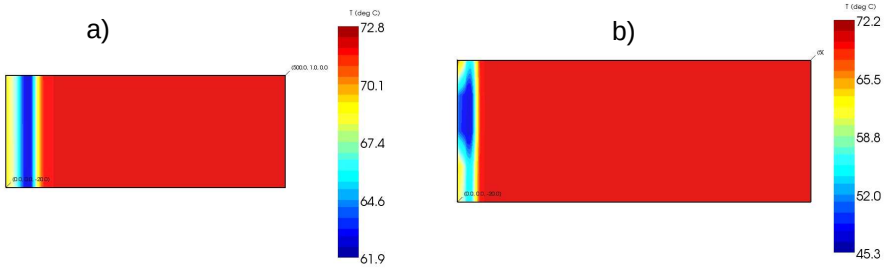

Fig. 23: Temperature profiles in the reservoir following CO2 injection (Tinj=80℃) for a continuous injection rate of 8 kg/s.

3.5.5.4 Conclusions

- A reservoir simulator has been set up allowing simulation/prediction of several key near-well processes occurring during injection of CO_2 in depleted gas fields.
- Generic sensitivity studies have been performed with the simulator for a sandstone reservoir with parameter values representative of depleted gas fields in the Netherlands.
- Results show that porosity reduction associated with formation dry-out and ensuing salt precipitation likely is rather small (< 1%) and largely controlled by residual brine content of the reservoir before injection and its salinity. Porosity reduction is largely independent of injection rate and temperature. Detailed information on brine content and brine salinity and its distribution within the reservoir is essential for reliable prediction of site-specific porosity reduction at injection sites.
- Generic modelling further shows that reservoir cooling due to CO_2 expansion during injection in a low-pressure sandstone reservoir (Joule Thomson effect) can reach

magnitudes of several tens of ^{0}C. Strong cooling is favoured by high injection rates, low permeability and cold injection temperature of the CO_2. Risk of pore clogging and permeability reduction due to brine freezing therefore only seems to occur when injection temperatures are very low.

- Model performance regarding the above processes still needs to be evaluated/validated with respect to laboratory experimental data and field observations.

3.6 Summary and future work

The UNIQUAC and Pitzer Gibbs excess energy models that describe vapour-liquid, liquid-liquid and solid-liquid, e.g. salt precipitation/dissolution, phase equilibria are currently being coded and will be available to all CATO2 participants. These models provide a more accurate description of phase equilibria than current reservoir simulators, which allows a better description of processes occurring when injecting CO_2 into an aquifer or depleted gas field.

The precipitation of salt in a sandstone core containing saline water induced by CO_2 injection will be investigated using computer simulations and visualization experiments. Preliminary results of the simulations indicate that gravity segregation effects play a major role in the experiments. The experimental set-up is currently under construction.

Data describing the displacement of (formation) water by CO_2 are scarce but are crucial for the design and for operating a CO_2 subsurface storage. Long-tube experiments are being designed to investigate the displacement and mass transfer processes between CO_2 and water in a prous medium.

A relationship that describes permeability for a medium with decreasing porosity due to salt precipitation is necessary for adequate modelling of CO_2 sequestration in saline water containing formations. This relationship is not yet available. Therefore, an experimental set-up has been constructed to investigate the decrease in permeability associated with the decrease in porosity caused by salt precipitation induced by CO_2 injection. The set-up is ready for use.

Representative samples of P18 Bunter sandstone reservoir rocks, and samples from equivalent sandstones in the Northern Eiffel (Western Germany), have been obtained. The petrological and transport properties of these samples are being characterized using X-ray diffraction (XRD), optical microscopy analysis and permeametry. This data is essential for the construction of any model predicting reservoir behaviour.

Experiments investigating chemical reactions in the CO_2 -reservoir rock – pore fluid are being performed under (P18) in-situ conditions. Detailed analysis of the reacted sample material is currently ongoing. The chemical reaction data provides a basis for the construction and calibration of models that predict the long-term effects of CO_2 sequestration in the P18 reservoir.

Preliminary modelling results show that heterogeneities and geochemical reactions influence the mass transfer of CO_2 on a small scale. These effects will have to be incorporated in reservoir simulations.

Reservoir simulations show that the mineralization of CO_2 plays a small, but significant, part when sequestering CO_2 in Rotliegend sandstone that is prevalently present in the Dutch subsurface. Long-term reservoir simulations will have to consider this process for an adequate description of the reservoir behaviour.

3.6.1.1 References

Abrams, D. S. and J. M. Prausnitz (1975). Statistical thermodynamics of liquid-mixtures - new expression for excess Gibbs energy of partly or completely miscible systems. AIChE Journal 21(1): 116-128.

Audigane, P., J. Lions et al. (2008) Geochemical modeling of CO_2 injection into a methane gas reservoir at the K12-B field, North Sea. In *Carbon dioxide sequestration in geological media - State of the science*. Grobe, M., Pashin, J.C., and Dodge, R.L. (eds): AAPG Studies 59,1-20.

Ames, R. and P.F. Farfan (1996). The environments of deposition of the Triassic Main Buntsandstein Formation in the P and Q quadrants, offshore the Netherlands. In: Rondeel et al. (eds.) “Geology of gas and oil in the Netherlands”, Kluwer Acad. Publish.

Bacci, G., A. Korre and S. Durucan (2011). Experimental investigation into salt precipitation during CO2 injection in saline aquifers. Proc. 10th Int. Conf. Green House Gas Technologies (GHGT-10), 19-23 September 2010, Amsterdam. Energy Procedia.

Bachu, S. and J.J. Adams (2003). Sequestration of CO2 in geological media in response to climate change: Capacity of deep saline aquifers to sequester CO2 in solution. Energy Conversion and Management 44: 3151–3175.

Bear, J. (1972). Dynamics of Fluids in Porous Media, Elsevier, New York.

Cantwell, W. (1992). Final Report of Mineralogy Analysis for Amoco Netherlands Petroleum Company, Well number P/18-2 and P/18-3, The Netherlands.

Farajzadeh, R. (2009). Enhanced Transport Phenomena in CO_2 sequestration and CO_2 EOR. PhD thesis, Delft University of Technology, Delft, The Netherlands.

Gaus, I. (2010). Role and impact of CO2-rock interactions during CO2 storage in sedimentary rocks. International Journal of Greenhouse Gas Control 4:73-89.

Gaus, I., M. Azaroual et al. (2005). Reactive transport modelling of the impact of CO2 injection on the clayey cap rock at Sleipner (North Sea). Chemical Geology 217: 319-337.

Hamer, W.J. and Y.Wu (1972) Osmotic Coefficients and Mean Activity Coefficients of Uni-univalent Electrolytes in Water at 25_C. Journal of Physical Chemistry Reference Data, 1: 1047–1099.

Hangx, S. J. T. and C. J. Spiers (2009). Reactions of plagioclase feldspars with CO_2 under hydrothermal conditions. Chemical Geology, 265(1-2): 88-98.

Hurter, S. and D. Labregere (2007) Simulation for CO_2 injection projects with compositional simulator, SPE108540

Li, Y.-K. and L.X. Nghiem (1986). Phase Equilibria of Oil, Gas and Water/Brine Mixtures from a Cubic Equation of State and Henry's Law. Canadian Journal Chemical Engineering, 486-496.

Liteanu E (2009). Subsurface impact of CO_2, response of carbonate rocks and wellbore cement to supercritical CO_2 injection and long-term storage. PhD thesis ISBN/EAN 978-90-5744-171-4

Müller, N., R. Qi, et al. (2009). CO_2 injection impairment due to halite precipitation. Energy Procedia, 1(1): 3507-3514.

Nghiem L, P. Sammon, J. et al. (2004). Modeling CO_2 storage in aquifers with a fully coupled geochemical EOS compositional simulator. SPE Paper 89474.

Nicolaisen, H., P. Rasmussen, et al. (1993). CORRELATION AND PREDICTION OF MINERAL SOLUBILITIES IN THE RECIPROCAL SALT SYSTEM (NA+, K+)(CL-, SO4(2-))-H2O AT 0-100-DEGREES-C. Chemical Engineering Science 48(18): 3149-3158.

Pape, H., C. Clauser, et al. (1999). Permeability prediction based on fractal pore-space geometry. Geophysics 64(5): 1447-1460.

Peach, C. J. (1991). Experimental Apparatus and Methods. Influence of deformation on the fluid transport properties of salt rocks. Phd Thesis, Geologica Ultraiectina, Utrecht University, Utrecht.

Pedersen, K.S., Aa. Fredensland, et al. (1984). Viscosity of crude oils. Chemical Engineering and Science 39: 1011–1016.

Peng, D.Y. and D.B. Robinson (1976). A New Two-Constant Equation of State. Industrial and Engineering Chemistry: Fundamentals 15: 59–64.

Peters, C.A. (2009). Accessibilities of reactive minerals in consolidated sedimentary rock: An imaging study of three sandstones. Chemical Geology 265: 198-208.

Pitzer K.S. (1973). Thermodynamics of electrolytes. I. Theoretical basis and general equations. The Journal of Physical Chemistry 77: 268-277.

Pruess, K., C. Oldenburg, et al. (1999) TOUGH2 User's Guide, Version 2.0, Lawrence Berkeley National Laboratory Report LBNL-43134.

Pruess, K. and N. Muller (2009). Formation dry-out from CO_2 injection into saline aquifers: 1. Effects of solids precipitation and their mitigation. Water Resources Research 45: 11.

Ranganathan, P., P. van Hemert, et al. (2011). Numerical Modeling of CO_2 Mineralisation during Storage in Deep Saline Aquifer. Proc. 10th Int. Conf. Green House Gas Technologies (GHGT-10), 19-23 September 2010, Amsterdam, Energy Procedia.

Sander, B., A. Fredenslund, et al. (1986). Calculation of vapor-liquid-equilibria in mixed-solvent salt systems using an extended UNIQUAC equation. Chemical Engineering Science 41(5): 1171-1183.

Spain, D.R. (1991). Top seal analysis of the Muschelkalk/Rot Formations, Amoco Netherlands P/15-14 Core (3117 m-3152.5 m), Southern Dutch North Sea. Amoco Production Research, Tulsa, Oklahoma.

Sphycher, N., and K. Pruess (2004) CO_2-H_2O Mixtures in the geological sequestration of CO_2. II. Partitioning in Chloride Brines at 12-100^oC and up to 600 bar. Lawrence Berkeley National Laboratory: Report LBNL-56334.

Tambach, T.J., T. Benedictus et al. (2009). Geochemical study of CO_2 injection into depleted gas fields in the Netherlands. Proceedings TOUGH Symposium 2009, Lawrence Berkeley National Laboratory, Berkeley, California, September 2009.

Tester, J. W. (1997). Thermodynamics and its applications. New Jersey, Prentice Hall PTR.

Thomsen, K. (2005). Modeling electrolyte solutions with the extended universal quasichemical (UNIQUAC) model. Pure and Applied Chemistry 77(3): 531-542.

Van Genuchten, M.T. (1980). A closed-form equation for predicting the hydraulic conductivity of unsaturated soils. Soil Science Society of American Journal 44: 892–898.

Wang Y., E. Mackie, et al. (2009). Experimental study on halite precipitation during CO_2 sequestration, International Symposium of the Society of Core Analysis, Noordwijk, The Netherlands.

Wilkinson M., R. Stuart Haszeldine, et al.(2009). CO_2–mineral reaction in a natural analogue for CO_2 storage-implications for modeling. Journal of Sedimentary Research, 79: 486–494.

Zuluaga E., and J.C. Monsalve (2003). Water vaporization in gas reservoirs. SPE Eastern Regional Meeting, 6-10 September 2003, Pittsburgh, Pennsylvania. SPE Paper 84829.

Zuluaga E., N.I. Muñoz, and G.A. Obando (2001). An experimental study to evaluate water vaporization and formation damage caused by dry gas flow in porous media. International Symposium on Oilfield Scale, 30-31 January 2001, Aberdeen, United Kingdom. SPE Paper 68335.

Appendix A: Pitzer and UNIQUAC equations

The main Pitzer equations are

Equation 1 for the osmotic coefficient, ϕ ,

$$(\phi-1)=-(\sum_i m_i)^{-1}\left(\frac{\partial\left(G^{E,m}/RT\right)}{\partial w_w}\right)_{T,P,n_i}$$

$$=\frac{2}{\sum_i m_i}\left(\begin{array}{l}\frac{-A_\phi I^{3/2}}{1+bI^{1/2}}+\sum_c\sum_a m_c m_a\left(B^\phi_{ca}+ZC^\phi_{ca}\right)\\+\sum_{c<c'}\sum m_c m_{c'}\left(\Phi^\phi_{cc'}+\sum_a m_a\Psi_{cc'a}\right)\\+\sum_{a<a'}\sum m_a m_{a'}\left(\Phi^\phi_{aa'}+\sum_c m_c\Psi_{aa'c}\right)\\+\sum_n\sum_c m_n m_c\lambda_{nc}+\sum_n\sum_a m_n m_a\lambda_{na}++\sum_{n<n'}\sum m_n m_{n'}\lambda_{nn'}\\+\frac{1}{2}\sum_n m_n^2\lambda_{nn}\ldots\end{array}\right)$$

Equation 2 for the activity coefficient of cation M, γ_M ,

$$\ln\gamma_M=\left(\frac{\delta G^{E,m}/RT}{\delta n_M}\right)_{T,P,w_w,n_i\neq M}$$

$$=z_m^2F+\sum_a m_a\left(2B_{Ma}+ZC_{Ma}\right)+\sum_c m_c\left(2\Phi_{Mc}+\sum_a m_a\Psi_{Mca}\right)$$

$$+\sum_{a<a'}\sum m_a m_{a'}\Psi_{Maa'}+z_M\sum_c\sum_a m_c m_a C_{ca}+2\sum_n m_n\lambda_{nM}+\ldots$$

Equation 3 for the activity coefficient of anion X, γ_X ,

$$\ln\gamma_X=\left(\frac{\delta G^{E,m}/RT}{\delta n_X}\right)_{T,P,w_w,n_i\neq X}$$

$$=z_X^2F+\sum_c m_c\left(2B_{cX}+ZC_{cX}\right)+\sum_a m_a\left(2\Phi_{Xa}+\sum_c m_c\Psi_{cXa}\right)$$

$$+\sum_{c<c'}\sum m_c m_{c'}\Psi_{ccX'}+\left|z_X\right|\sum_c\sum_a m_c m_a C_{ca}+2\sum_n m_n\lambda_{nX}+\ldots$$

The mean activity coefficient for the electrolyte $M_{vc}X_{va}$ in a mixture is given by

Equation 4 for the activity coefficient of dissolved salt MX

$$\ln\gamma_{MX} = |z_M z_X| F + \frac{\upsilon_M}{\upsilon}\sum_a m_a\left(2B_{Ma} + ZC_{Ma} + 2\frac{\upsilon_X}{\upsilon}\Phi_{Xa}\right) + \sum_{a<a'}\sum m_a m_{a'}\frac{\upsilon_M}{\upsilon}\Psi_{Maa'}$$
$$+\frac{\upsilon_X}{\upsilon}\sum_c m_c\left(2B_{cX} + ZC_{cX} + 2\frac{\upsilon_c}{\upsilon}\Phi_{Mc}\right) + \sum_{c<c'}\sum m_c m_{c'}\frac{\upsilon_X}{\upsilon}\Psi_{ccX'}$$
$$+\sum_c\sum_a m_c m_a \upsilon^{-1}\left(2\upsilon_M z_M C_{ca} + \upsilon_M\Psi_{Mca} + \upsilon_X\Psi_{caX}\right) + \frac{2}{\upsilon}\sum_n m_n\left(\upsilon_M\lambda_{nM} + \upsilon_X\lambda_{nX}\right)$$

The parameters of the Pitzer equations are

- F includes the Debye-Hückel term and other terms,
- z_a is the charge of ion a,
- v_a is the number of ions in the solid salt with $v = v_M + v_X$,
- B_{ca} is an empirical parameter related to the interaction energy of the c and a ions (binary),
- C_{ca} is an empirical parameter related to the interaction energy of c and a ions (ternary)
- $\Psi_{cc'a}$ is an empirical parameter related to the interaction of c, c' and a ions
- Z is given by $\sum_i m_i |z_i|$,
- $\Phi_{cc'}$ is an empirical parameter related to interactions between c and c' or a and a'

The UNIQUAC model equations are

Equation 5: The symmetric rational activity coefficient of water, γ_w, in the UNIQUAC model

$$\ln\gamma_w = \ln\gamma_w^{DH} + \ln\frac{\phi_w}{x_w} + 1 - \frac{\phi_w}{x_w} - \frac{z}{2}q_w\left[\ln\frac{\phi_w}{\theta_w} + 1 - \frac{\phi_w}{x_w}\right] + q_w\left[1 - \ln\left(\sum_k\theta_k\psi_{ki}\right) - \sum_k\frac{\theta_k\psi_{wk}}{\sum_l\theta_l\psi_{lk}}\right]$$

Equation 6: The unsymmetric (denoted by *) rational activity coefficient of ion I, γ_i^*, in the UNIQUAC model

$$\ln\gamma_i^* = \ln\gamma_i^{*,DH} + \ln\frac{\phi_i}{x_i} - \frac{\phi_i}{x_i} - \ln\frac{r_i}{r_w} + \frac{r_i}{r_w} - \frac{z}{2}q_i\left[\ln\frac{\phi_i}{\theta_i} - \frac{\phi_i}{x_i} - \ln\frac{r_i q_w}{r_w q_i} + \frac{r_i q_w}{r_w q_i}\right] +$$
$$q_i\left[-\ln\left(\sum_k\theta_k\psi_{ki}\right) - \sum_k\frac{\theta_k\psi_{ik}}{\sum_l\theta_l\psi_{lk}} + \ln\psi_{wi} + \psi_{iw}\right]$$

The parameters of the UNIQUAC model equations are

- γ_n^{DH} is the activity coefficient of component n from the extended Debye-Hückel equation
- ϕ_n is the volume fraction of species n
- x_n is the mole fraction of species n

- q_w is an empirical parameter related to the volume of molecule of component n
- r_w is an empirical parameter related to the surface area of molecule of component n
- z is the theoretical coordination number (set at 10)
- θ_n is the surface area fraction of species n